Supplementary Information

Water Soluble Palladium(II) and Platinum(II) Acyclic Diaminocarbene Complexes: solution behavior, DNA Binding, and Antiproliferative Activity

Tatiyana V. Serebryanskaya,[a] Mikhail A. Kinzhalov,[b] Vladimir Bakulev,[b] Georgii Alekseev,[b] Anastasiya Andreeva,[b] Pavel V. Gushchin,[b] Aleksandra V. Protas,[b] Andrey S. Smirnov,[b] Taras L. Panikorovsky,[b] Petra Lippman,[c] Ingo Ott,[c] Cyril M. Verbilo,[a] Alexander V. Zuraev,[a] Alexander S. Bunev,[d] Vadim P. Boyarskiy,[b] Nina A. Kasyanenko[b]

[a]*Research Institute for Physical Chemical Problems, Belarusian State University, Leningradskaya 14, 220006 Minsk, Belarus. E-mail: serebryanskaya.t@gmail.com;*
[b] *Saint Petersburg State University, St. Petersburg State University, 7/9 Universitetskaya nab., St. Petersburg, 199034 Russia. E-mails: m.kinzhalov@spbu.ru, v.boiarskii@spbu.ru;*
[c] *Institute of Medicinal and Pharmaceutical Chemistry, Technische Universität Braunschweig, Beethovenstrasse 55, D-38106 Braunschweig, Germany;*
[d] *Medicinal Chemistry Center, Togliatti State University, Belorusskaya 14, 445020 Togliatti, Russia.*

Table of contents

S1. Materials and instrumentation

Reagents and materials used. Solvents, $PdCl_2$, 1,2-diaminobenzene, and isocyanides were obtained from commercial sources and used as received, whereas $CHCl_3$ was purified by the conventional distillation over calcium chloride. Complexes **1a**,**b** and **2a**,**b** were prepared by the known procedures [1, 2]. Compounds **4a**,**b** [1], **1c** [3, 4] and **2c** [3, 4] were prepared as described earlier.

Instrumentation and methods. C, H, and N elemental analyses were carried out on a Euro EA 3028HT CHNSO analyzer. Mass spectra were obtained on a Bruker micrOTOF spectrometer equipped with electrospray ionization (ESI) source and MeOH was used as the solvents. The instrument was operated both at positive and negative ion modes using *m/z* range of 50–3000. The capillary voltage of the ion source was set at –4500 V (ESI^+) or 3500 V (ESI^-) and the capillary exit at ±(70–150) V. The nebulizer gas pressure was 0.4 bars and drying gas flow 4.0 L/min. The most intensive peak in the isotopic pattern is reported. Infrared spectra (4000–400 cm^{-1}) were recorded on a Shimadzu FTIR 8400S instrument in KBr pellets. ^1H, $^{13}C\{^1H\}$, $^{195}Pt\{^1H\}$ NMR spectra were acquired on a Bruker Avance 400 spectrometers at ambient temperature. The solid-state NMR experiments were performed on a Bruker Avance III NMR 400 WB spectrometer operating at 9.4 T. The CP/MAS NMR spectra were acquired using a double-resonance 4 mm MAS Bruker probe at a resonance frequency of 162 MHz under 14 kHz MAS. ^{195}Pt CP/MAS NMR spectra were acquired using a direct excitation technique (DE). The CP contact time in all experiments was 3.5 μs with a delay between acquisitions of 1 sec and number of scans was collected 20000.

X-ray Structure Determinations. For a single crystal X-ray diffraction experiment, crystals of **4a**•1½CH_2Br_2•H2O and **5a**•H_2O was fixed on a micro mount and placed on Agilent Technologies SuperNova diffractometer and measured at the temperature of 100K using monochromated CuKα radiation. The unit cell parameters and the refinement parameters are given in **Table S1**. The structures has been solved by the means of the Superflip [5] structure solution program using Charge Flipping and refined by SHELXL program [6] incorporated in the OLEX2 program package [7]. The carbon-bound H atoms were placed in calculated positions and were included in the refinement in the 'riding' model approximation, with $U_{iso}(H)$ set to $1.5U_{eq}(C)$ and C–H 0.96 Å for the CH_3 groups, $U_{iso}(H)$ set to $1.2U_{eq}(C)$ and C–H 0.93 Å for the CH groups, N–H 0.90 Å with $U_{iso}(H)$ set to $1.2U_{eq}(N)$ for the NH_2 group and N–H 0.86 Å with $U_{iso}(H)$ set to $1.2U_{eq}(N)$ for the NH group. Empirical absorption correction was applied in CrysAlisPro (Agilent Technologies, Version 1.171.36.20, release 27-06-2012) program complex using spherical harmonics, implemented in SCALE3 ABSPACK scaling algorithm. The SQUEEZE routine from PLATON [8] was applied to the data to account for the solvent void within the lattice. Void spaces with a total void volume of 353 $A^{\circ -3}$ and a sum of 281 ē were accounted within the unit cell. This could be accounted for by the inclusion of three molecules of dibromomethane per unit cell. Supplementary crystallographic data for this paper have been deposited at Cambridge Crystallographic Data Centre (CCDC 1535469 for **4a**•1½CH_2Br_2•H_2O and 1502101 for **5a**•H_2O) and can be obtained free of charge via www.ccdc.cam.ac.uk/data_request/cif.

Cell culture. HT-29 colon carcinoma cells, MDA-MB-231 breast cancer cells, MCF-7 breast carcinoma cells and L929 mouse fibroblast cells were maintained in Dulbecco's modified Eagle's medium (DMEM; 4.5 gL^{-1} d-glucose, l-glutamine, pyruvate), supplemented with gentamycin (50 mgL^{-1}) and fetal bovine serum superior, standardized (Biochrom GmbH, Berlin) (10% v/v), with

a weekly passage. RC-124 healthy human kidney cells were maintained in McCoy's 5A medium (modified with l-glutamine) supplemented with gentamycin (50 mgL^{-1}) and fetal bovine serum superior, standardized (Biochrom GmbH, Berlin) (10% v/v), and had also one passage a week. For experiments with RC-124 cells, the flasks or microtiter plates were pretreated as follows: 1.5% (m/v) sterilized gelatine solution (10 mL for cell culture flasks, 30 μL for microtiter plates) was added to each flask or well and incubated for 1 h at 37 °C. The excess solution was then removed, the flasks or wells were washed with PBS (pH 7.4), and the new cell culture medium was added.

SK-OV-3 ovarian adenocarcinoma cells, MCF7 breast carcinoma cells, HT-1080 fibrosarcoma cells, A549 lung adenocarcinoma cells and HEK293 embryonic kidney cells were purchased from the ATCC. HT-1080 and HEK293 cells were maintained in EMEM (Gibco, UK) supplemented with 10% fetal bovine serum (FBS, Gibco, UK), penicillin (100 UI mL^{-1}), streptomycin (100 μg mL^{-1}), amphotericin B (2.5 μg mL^{-1}), and *L*-glutamine (2 mM). MCF-7 cells were maintained in DMEM (Gibco, UK) supplemented with 10% fetal bovine serum (FBS, Gibco, UK), penicillin (100 UI mL^{-1}), streptomycin (100 μg mL^{-1}), amphotericin B (2.5 μg mL^{-1}), *L*-glutamine (4 mM), and human recombinant insulin (10 μg mL^{-1}). SK-OV-3 cells were maintained in McCoy's 5A medium (Gibco, UK) supplemented with 10% fetal bovine serum (FBS, Gibco, UK), penicillin (100 UI mL^{-1}), streptomycin (100 μg mL^{-1}), amphotericin B (2.5 μg mL^{-1}), and *L*-glutamine (1.5 mM). A549 lung adenocarcinoma cell were maintained in F12 medium (Gibco, UK) supplemented with 10% fetal bovine serum (FBS, Gibco, UK), penicillin (100 UI mL^{-1}), streptomycin (100 μg mL^{-1}), amphotericin B (2.5 μg mL^{-1}), and *L*-glutamine (1 mM). All cells line cultivation under a humidified atmosphere of 95% air/5% CO_2 at 37 °C. Subconfluent monolayers, in the log growth phase, were harvested by a brief treatment with TrypLE Express solution (Gibco) in phosphate buffered saline (PBS, Capricorn Scientific, Germany) and washed three times in serum-free PBS. The number of viable cells was determined by trypan blue exclusion.

Crystal violet assay. The antiproliferative effects were determined according to a recently used method with minor modifications.[9] Briefly, 100 μL of HT-29 cells (2565 cells mL^{-1}), MDA-MB-231 cells (4120 cells mL^{-1}), MCF-7 cells (4840 cells mL^{-1}), or RC-124 cells (1460 cells mL^{-1}) were transferred into the wells of 96-well microtiter plates and incubated at 37°C under 5% CO2 for 72 h (MCF-7, MDA-MB-231, RC-124) or 48 h (HT-29, L929). Stock solutions of the compounds in dimethylformamide (DMF) were freshly prepared and diluted with the respective cell culture medium to graded concentrations (final concentration of DMF: 0.1% v/v). After 72 h (HT-29, L929) or 96 h (MCF-7, MDA-MB-231, RC-124) of exposure, the cell biomass was determined by crystal violet staining, and the IC_{50} value was determined as the concentration that caused 50% inhibition of cell proliferation compared to an untreated control. Results were calculated as the mean values of three independent experiments.

MTT assay. The effects of the synthesized compounds and cisplatin on cell viability were determined using the MTT colorimetric test. All examined cells were diluted with the growth medium to 6×10^4 cells per mL and the aliquots (6×10^3 cells per 100 μL) were placed in individual wells in 96-multiplates (Eppendorf, Germany) and incubated for 24 h. The next day the cells were then treated with cisplatin, 4a and 5a compounds, separately at varying concentrations and incubated for 72 h at 37 °C). Each compound was tested in triplicate. After incubation, the cells were treated with 40 μL MTT solution (3-(4,5-dimethylthiazol-2-yl)-2,5-diphenyltetrazolium bromide, 5 mg mL^{-1} in PBS) and incubated for 4 h. After an additional 4h incubation, the medium with MTT was removed and DMSO (200 μL) was added to dissolve the crystals formazan. The

plates were shaken for 10 min. The optical density of each well was determined at 560 nm using a microplate reader GloMax Multi+ (Promega, USA). Each of the tested complexes was evaluated for cytotoxicity in three separate experiments. The results are given in Table S4.

Proapoptotic activity assay. For the detection of apoptosis, the cells were plated at 6-well culture plates (Eppendorf, Germany) and allowed to grow overnight. After the cells reached subconfluency, the medium was replaced with tested complexes (EC_{50} for examined cell line). The exposed cells were placed at 37 °C in a 5% CO_2 incubator for 48 h. The cultured cells were washed twice with PBS and resuspended in 1× binding buffer (AnnexinV-FITC kit, Invitrogen, USA) at a concentration 1×10^6 mL^{-1}. Annexin FITC and propidium iodide (PI) were added to 100 μL of the cell suspension and incubated for 15 min at room temperature (25 °C) in the dark. After incubation 400 μL of 1× binding buffer was added to each tube and the stained cells were analyzed within 1 h using CytoFlex (Beckham Culture, USA) and CytExpert 2.1 program. Since, Annexin V FITC staining precedes the loss of membrane integrity that accompanies the later stage identified by PI, Annexin FITC positive, PI negative indicates early apoptosis, while the viable cells are Annexin V FITC negative, PI negative. The cells that are in late apoptosis, or dead are both Annexin V FITC and PI positive.

Cell cycle analysis. The cells were plated at 6-well culture plates (Eppendorf, Germany) and allowed to grow overnight. After the cells reached subconfluency, the medium was replaced with tested complexes (EC_{50} for examined cell line). The exposed cells were placed at 37 °C in a 5% CO_2 incubator for 48 h. The cultured cells were washed twice with PBS and then fixed with 70% ethanol in PBS. Fixed cells were collected and washed with PBS and resuspended in 200 μL Guava cell cycle reagent (Merck Millipore, USA) for DNA staining. After the stained cells were analyzed using CytoFlex (Beckham Culture, USA) and CytExpert 2.1 program.

DNA binding studies. Interaction of complexes **4a** and **5a** with calf thymus (CT) DNA ("Sigma") was studied using absorption and circular dichroism (CD) spectroscopy, low-gradient viscometry, flow birefringence, fluorescence spectroscopy, atomic force microscopy. Molecular weight of CT DNA (10^7 g/mol) was found from DNA intrinsic viscosity in 0.15 M NaCl [10]. The stock solutions of **4a** and **5a** (10^{-4} M) were prepared in 5 mM NaCl. Measurements were performed at 21 °C. Details of hydrodynamic measurements are given in Supplementary data.

Spectral studies. Concentration of CT DNA in solutions was determined from the difference in the absorbance of hydrolyzed solutions in the presence of 4% $HClO_4$ at wavelengths λ = 270 and 290 nm. The native state of DNA was checked by hyperchromic effect upon denaturation of the macromolecule. The final samples were prepared by mixing the equal volumes of CT DNA solution and ADC complex solutions in 5 mM NaCl. The absorption spectra in the range 230–350 nm were recorded on SF56 (Russia) and Specord 2000 spectrophotometers using quartz cuvette (1 cm path length). Circular dichroism (CD) spectra in the range 230–340 nm were recorded with a Jobin–Yvon Mark IV autodichrograph and are given in the units of extinction $M^{-1}cm^{-1}$. For the competitive binding experiments, the complexes of CT DNA with ADC compounds or *cis*-DDP were incubated at 4 °C for 24 h; then the solution of *cis*-DDP or the corresponding ADC complex, respectively, was added, and UV spectra were taken. The r_i values are given for the final solutions.

Thermal denaturation study. DNA melting was studied with Specord 2000 spectrophotometer in 1 cm quartz quiet. The melting temperature of DNA refers to the temperature at which 50% of DNA hydrogen links between base pairs are being destroyed. T_m is the middle point of the

transition, fixed by the appearance of a hyperchromism of 260 nm (the maximum of the DNA absorption band).

Atomic force microscopy. The AFM images of DNA and its complexes with ADC compounds were obtained on the surface of fresh cleaved mica with Bruker Multimode 8 equipment operated in ScanAssist-Air mode. The samples were prepared using the following standard procedure: a drop of the solution was placed on mica substrates; in 2 minutes, the substrate was washed with distilled water and dried in vacuum.

Fluorescence spectroscopy. The fluorescence of solutions was measured with a Hitachi-850 spectrofluorometer using a 1 cm quartz cuvette after the solutions were held for 1 h at the ambient temperature. Luminescence excitation and the emission spectra were corrected for the spectral sensitivity of the instrument.

Low-gradient viscometry. The relative viscosities of DNA solutions η_r were determined on a low-gradient rotational viscometer of the Zimm–Crothers type [11].

The relative solution viscosity $\eta_r = \frac{\eta}{\eta_0}$ (where η and η_0 are the viscosities of the solution and the solvent respectively) was measured at different velocity gradients g in the range of 0.5 - 2 s^{-1} and averaged since its extrapolation to $g = 0$ is not required because of the absence of a gradient dependence. The intrinsic viscosity $[\eta] = \lim_{c \to o}\left(\frac{\eta_r - 1}{c}\right)$ is related to DNA parameters by the Flory's formula:

$$[\eta] = \frac{\Phi\left\langle h^2 \right\rangle^{\frac{3}{2}}}{M} = \Phi \frac{(L2p)^{3/2}}{M}\alpha^3, \qquad (1)$$

where Φ is the Flory coefficient, which depends on solvent quality and the rigidity of macromolecules [12], M is the molecular mass of DNA, L is the hydrodynamic length of the double helix, α is the coefficient of linear swelling describing the volume effect including the polyelectrolyte swelling. The parameter $\langle h^2 \rangle^{1/2}$ (the mean square distance between the ends of the polymer chain) defines the linear size of the molecular coil. In a solution with a good solvent the equation $\langle h^2 \rangle^{1/2} = \alpha(LA)^{1/2}$ is correct. The Kuhn's model of freely jointed segments can be used for DNA with $M > 2\times10^6$. The average value of the length of the Kuhn's statistical segment A indicates the chain rigidity. The DNA rigidity of DNA can be also defined via the persistent length $p = A/2$.

Flow birefringence. The birefringence values Δn of DNA solutions were measured in a field of flow velocity gradient g, which provides the orientation of ellipsoidal molecular coils. The value $\frac{(\Delta n/g)_{g\to o}}{(\eta_r - 1)\eta_0}$ ($\Delta n/g$) for $g \to 0$ was used to calculate the value that can determine the optical anisotropy of DNA statistical segment (α_1-α_2), i.e. the difference between the polarizabilities of the segment along and normal to the axis of the DNA helix [13]:

$$\frac{(\Delta n/g)_{g\to o}}{(\eta_r - 1)\eta_0} = \frac{4\pi}{45kTn_s}\frac{(n_s^2 - 1)^2}{n_s}(\alpha_1 - \alpha_2). \qquad (2)$$

Value $(\alpha_1-\alpha_2) = S\Delta\beta = (A/l)\Delta\beta$, where S is the number of base pairs in the statistical segment

with the average length A, l is the base pair length along the DNA axis (0.34 nm), $\Delta\beta$ - is the optical anisotropy of a base pair (difference in the its polarizabilities along and normal to the axis of the DNA helix).

Molecular docking studies. Molecular docking experiment was performed by using Autodock 4.2.6 and AutoDockTools 4 [14]. This program offers different algorithms for docking studies based on empirical scoring functions along with precomputation of grid of potentials for different types of atoms. We have chosen LGA (Lamarckian genetic algorithm) for further investigations with standard parameters and 100 conformations generation, as this algorithm combines features of local search and global search. Due to absence of palladium(II) and platinum(II) parameters in default scoring functions (Lennard-Jones (LJ) potential parameters, solvation parameters) LJ parameters were taken elsewhere [15] and added manually. Solvation parameter was taken similar to other dication species in AutoDock parameter library.

Protein structures were extracted from The Protein Data Bank [16]. All ligands and water molecules were deleted form the structures, charges were added for all atom depending on standard charges of each nucleotides atoms (Kollman charges). In case of intercalation docking was performed in a box of 16Å×16Å×16Å centered on intercalating gap with 0.2 Å spacing. Minor groove docking was performed in a box of 24Å×24Å×24Å, placed all over the structure with 0.2 Å spacing.

Crystal structure of 4a was used to study binding of dicationic form of 4a. The structure of monocationic form of 4a was optimized using Gaussian 16 software package [17]. Geometry optimization was performed using the DFT method with PBE1PBE [18] hybrid functional and 6-311+G(d)[] basis set for all atoms except palladium. The LANL2DZ [19] basis set with pseudopotentials was used for the palladium atom. Partial atomic charges for both forms of 4a were obtained by quantum chemistry calculations and used in docking study as algorithms of AutoDockTools 4 are unable of assigning partial atomic charges to atoms of metal complexes.

Visualization was performed using USCF Chimera [20].

S2. Structure determination of new complexes 4c and 5a–c

New complexes **4c** and **5a**–**c** were obtained as white solids and were characterized by elemental analyses (C, H, N), high resolution ESI^+-MS, and IR and ^1H NMR spectroscopies. Complex **5a** was also characterized by $^{13}C\{^1H\}$ and $^{195}Pt\{^1H\}$ NMR spectroscopies; complexes **4c** and **5c** – by $^{19}F\{^1H\}$ NMR spectroscopies. Unfortunately, complex **5b** is unstable in concentrated solutions in MeOH and decomposes forming Pt black in a few minutes at RT, which greatly complicates the registration of its $^{13}C\{^1H\}$ and $^{195}Pt\{^1H\}$ NMR spectra. However, there is no change in diluted solutions (5 mg/ml) in the presence of a tenfold excess of Me_4NCl for 2 weeks. Complex **5b** is unstable in solutions and decomposes forming Pt black in a few minutes at RT.

Complexes **5a,b** gave satisfactory C, H, and N elemental analyses, which are consistent with the proposed formulas. The $HRESI^+$ mass spectra of **4c** and **5a**–**c** demonstrated the corresponding $[M–Cl]^+$ and $[M–2Cl–H]^+$ ions along with the characteristic isotopic distribution. In addition, the *m/2* peaks from $[M–2Cl]^{2+}$ were observed in the mass spectra of **4c** and **5a–c**. The IR spectra of **4c** and **5a**–**c** indicated formation of the carbene moiety, thus, intense absorption at 1570–1545 cm^{-1} was assigned to $\nu(N–C_{carbene})$ and corresponding $\nu(N–H)$ bands emerge in the range of 3250–3040 cm^{-1}, whereas $\delta(N–H)$ is closer to 1500 cm^{-1}. The IR spectra of **4c** and **5a**–**c** display no bands in the range between 2300 and 2190 cm^{-1} due to $\nu(C{\equiv}N)$, thus collaterally supporting the transformation of both isocyanide ligands into aminocarbenes.

There are no signals from the NH protons of the carbene fragments and the amino groups in the ^1H NMR spectra of **4 a**–**c** and **5a**–**c**. The reason is their acidic character afforded easy H/D exchange with the deuterated solvent. The $HRESI^+$ mass spectra of **4a** and **5a** in CD_3OD demonstrated the corresponding $[M–Cl+8]^+$ and $[M–2Cl–H+7]^+$ ions along with the characteristic isotopic distribution that confirmed replacing all 8 NH protons.

The $^{13}C\{^1H\}$ NMR data also confirmed the structures of the synthesized species. Addition of 1,2-diaminobenzene to **2a** is accompanied by a pronounced downfield shift of both of the isocyanide quaternary C atom signals to the range common for metal-bonded ADC (δ_C 160–224 ppm). [21-25] In **5a**, the $C_{carbene}$ ^{13}C signal was found to resonate at δ_C 174 ppm; that is *ca*. 60 ppm downfield shifted *vs*. signals in the starting **2a**. $^{195}Pt\{^1H\}$ NMR spectrum of **5a** exhibits a signal at –3778 ppm which is consistent with the literature data for Pt(II) in the related coordination environment.

$^{19}F\{^1H\}$ NMR spectra of **4c** and **5c** show 3 singlets with an intensity ratio of ca. 1 : 10 : 1, which probably corresponds to a mixture of a symmetrical bischelate form and an asymmetrical monochelate form.

S3. X-ray structure determination

Table S1. Crystal data and structure refinement for **4a**•1½CH_2Br_2•H_2O and **5a**•H_2O.

Ide ntification code	**4a**•1½CH_2Br_2•H_2O	**5a**•H_2O
Empirical formula	$C_{63}H_{78}Br_6Cl_4N_{12}O_2Pd_2$	$C_{30}H_{36}Cl_2N_6OPt$
Temperature/K	100(2)	100(2)
Crystal system	triclinic	triclinic
Space group	*P*-1	*P*-1
a/Å	12.1819(8)	12.1790(6)
b/Å	12.3676(7)	12.3643(3)
c/Å	12.8999(7)	12.9592(4)
α/°	66.979(5)	66.866(3)
β/°	84.114(5)	84.414(3)
γ/°	75.288(5)	75.822(3)
Volume/Å^3	1730.07(19)	1739.88(12)
Z	1	2
ρ_{calc}g/cm^3	1.794	1.456
μ/mm^{-1}	10.090	9.189
F(000)	926.0	756.0
Crystal size/mm^3	0.1 × 0.05 × 0.05	0.2 × 0.18 × 0.15
Radiation	Cu*K*α (λ = 1.54184)	Cu*K*α (λ = 1.54184)
2Θ range for data collection/°	7.446 to 139.984	7.418 to 144.986
Index ranges	-13 ≤ h ≤ 14, -10 ≤ k ≤ 15, -11 ≤ l ≤ 15	-15 ≤ h ≤ 14, -15 ≤ k ≤ 14, -15 ≤ l ≤ 16
Reflections collected	13236	16339
Independent reflections	6532 [R_{int} = 0.0464, R_{sigma} = 0.0517]	6868 [R_{int} = 0.0684, R_{sigma} = 0.0683]
Data/restraints/parameters	6532/0/425	6868/0/326
Goodness-of-fit on F^2	1.024	1.073
Final *R* indexes [I>=2σ (I)]	R_1 = 0.0708, wR_2 = 0.1945	R_1 = 0.0643, wR_2 = 0.1723
Final *R* indexes [all data]	R_1 = 0.0778, wR_2 = 0.2080	R_1 = 0.0706, wR_2 = 0.1763
Largest diff. peak/hole / e Å^{-3}	2.56/-1.24	2.53/-1.51

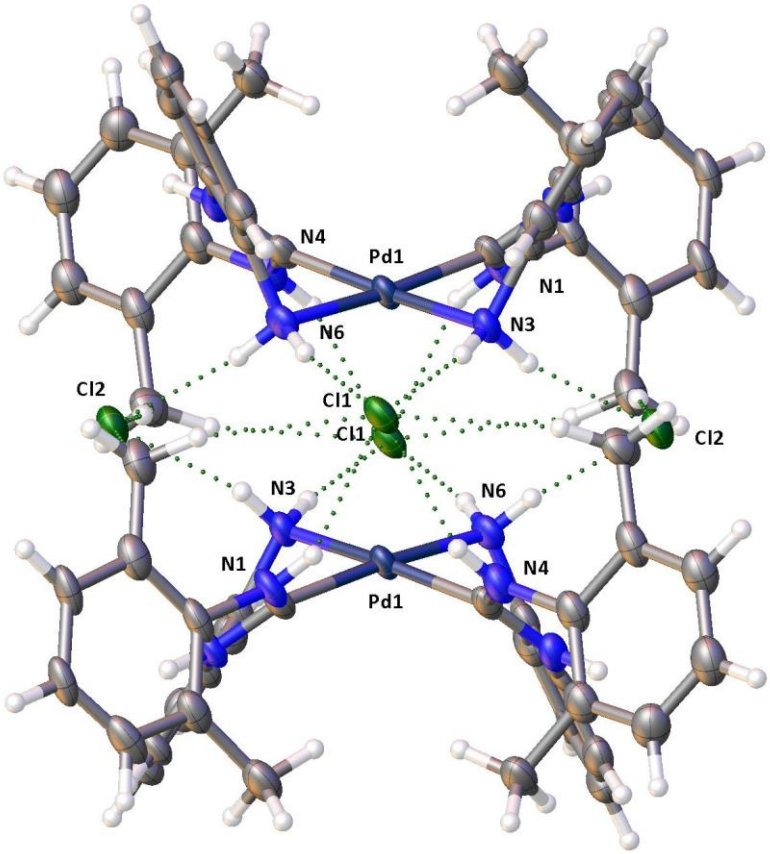

Figure S1. View of **4a**•1½CH_2Br_2•H_2O with the intermolecular hydrogen bonds.

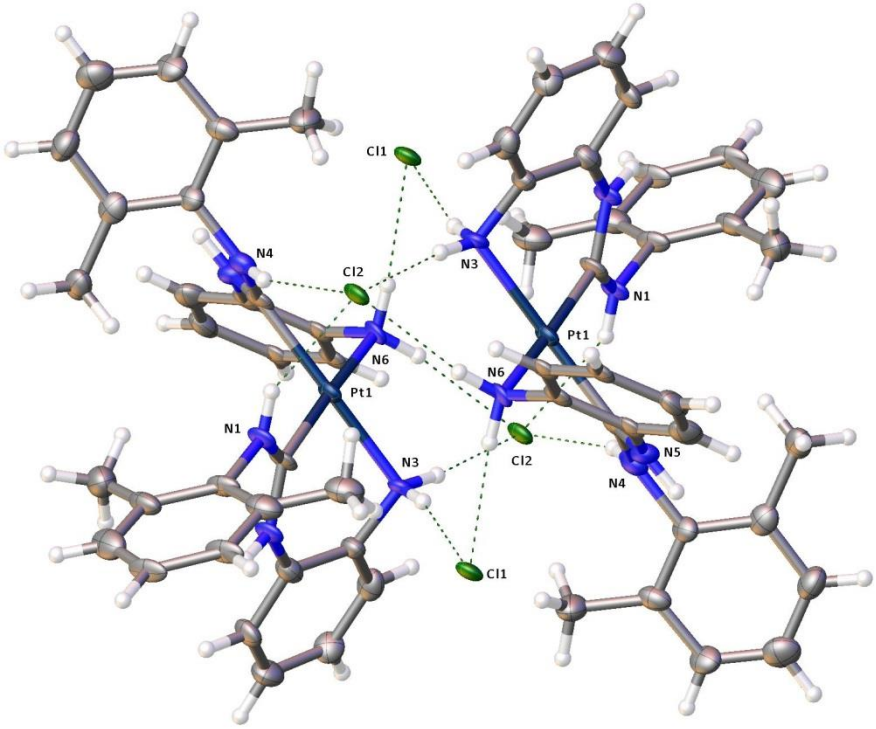

Figure S2. View of **5a**•H_2O with the intermolecular hydrogen bonds.

Table S2. Selected bond lengths (Å) and angles (°) for **4a**•1½CH_2Br_2•H_2O and **5a**•H_2O.

Bond or angle	**4a**•1½CH_2Br_2•H_2O	**5a**•H_2O
M1–C1	2.023(6)	2.007(8)
M1–C16	2.018(6)	2.023(8)
M1–N3	2.086(5)	2.100(6)
M1–N6	2.112(5)	2.093(6)
C1–N1	1.311(9)	1.328(10)
C1–N2	1.354(8)	1.338(10)
N1–C2	1.450(8)	1.474(9)
N2–C10	1.395(9)	1.403(10)
C10–C15	1.411(9)	1.396(11)
C15–N3	1.446(7)	1.447(9)
C16–N4	1.300(9)	1.312(10)
C16–N5	1.363(9)	1.341(11)
N4–C17	1.445(9)	1.459(10)
N5–C25	1.441(9)	1.431(10)
C25–C30	1.397(10)	1.411(11)
C30–N6	1.459(9)	1.444(10)
C1–M1–C16	98.8(3)	100.6(3)
C1–M1–N3	84.3(2)	83.5(3)
N3–M1–N6	92.3(2)	92.4(2)
C16–M1–N6	84.0(2)	83.0(3)
N1–C1–N2	116.5(6)	116.2(7)
C1–N1–C2	126.5(5)	126.3(6)
C1–N2–C10	126.7(5)	126.9(6)
M1–N3–C15	108.1(4)	107.7(4)
N4–C16–N5	116.6(6)	118.2(7)
C16–N4–C17	127.4(6)	126.7(7)
C16–N5–C25	127.3(5)	129.0(7)
M1–N6–C30	106.0(4)	107.8(4)

Table S3. Hydrogen bonds for **4a**•1½CH_2Br_2•H_2O and **5a**•H_2O [Å and °][a]

N−H•••Cl	d(H•••A)	d(N•••Cl)	∠(N−H−Cl)
4a•1½CH_2Br_2•H_2O			
N(1)−H(1)•••Cl(1)	2.38	3.186(7)	153
N(3)−H(3A)•••Cl(1)#1	2.38	3.285(5)	172
N(3)−H(3B)•••Cl(2)#1	2.26	3.140(5)	164
N(4)−H(4)•••Cl(1)	2.36	3.192(7)	158
N(6)−H(6A)•••Cl(2)	2.25	3.154(6)	169
N(6)−H(6B)•••Cl(1)#1	2.35	3.253(6)	171
5a•H_2O			
N(1)−H(1)•••Cl(2)	2.42	3.203(7)	151
N(3)−H(3A)•••Cl(2)#1	2.42	3.299(6)	171
N(3)−H(3B)•••Cl(1)#1	2.29	3.157(7)	164
N(4)−H(4)•••Cl(2)	2.41	3.228(8)	159
N(6)−H(6A)•••Cl(1)	2.29	3.170(7)	168
N(6)−H(6B)•••Cl(2)#1	2.39	3.271(6)	172

[a] Symmetry transformations used to generate equivalent atoms: #1 $2 - x$, $2 - y$, $-z$.

S4. Stability and solution behavior in aqueous media studies

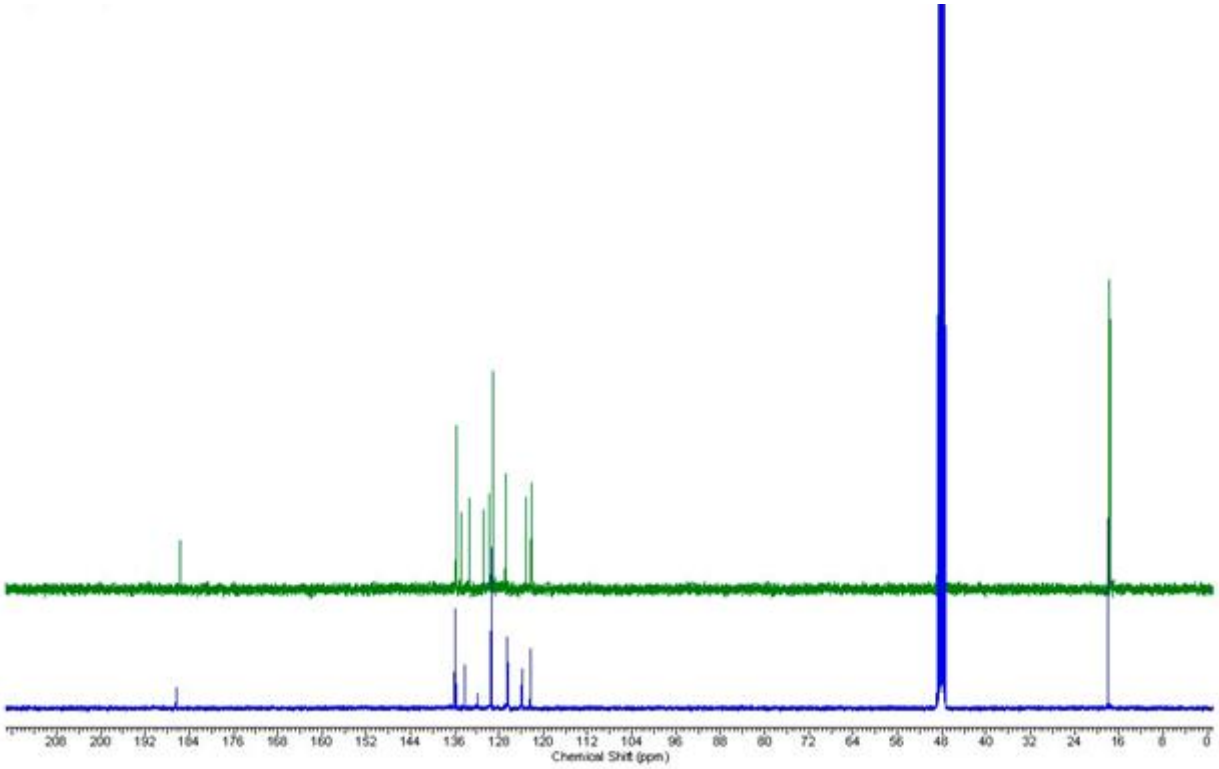

Figure S3. $^{13}C\{^{1}H\}$ NMR spectra of **4a** in D_2O/CD_3OD (4:1) mixture (top) and in CD_3OD (bottom).

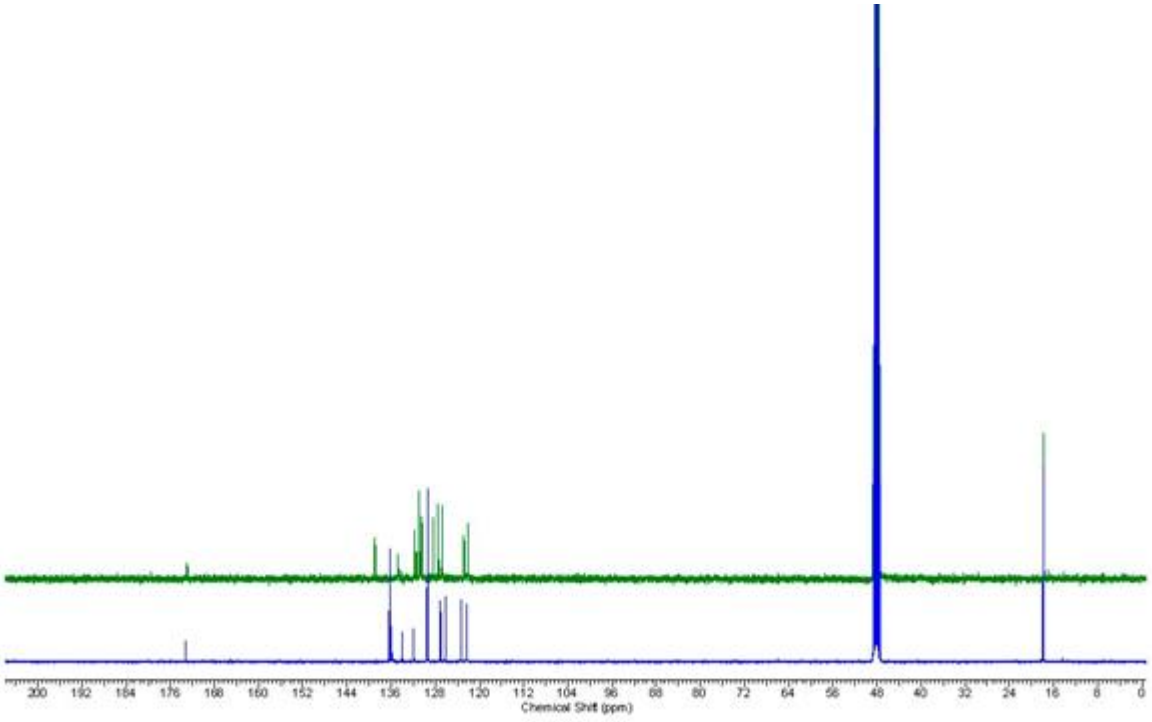

Figure S4. $^{13}C\{^{1}H\}$ NMR spectra of **5a** in D_2O/CD_3OD (4:1) mixture (top) and in CD_3OD (bottom).

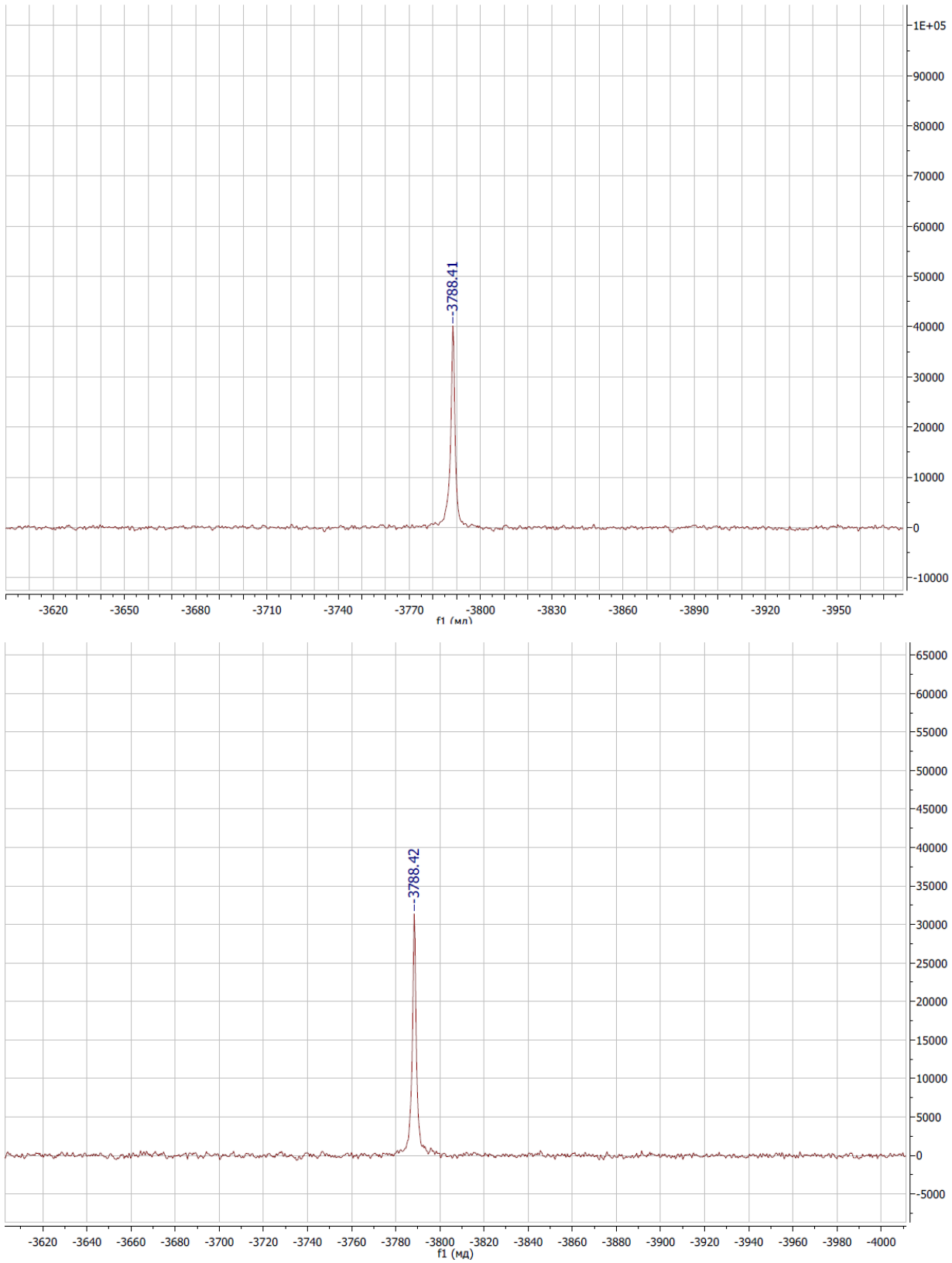

Figure S5. $^{195}Pt\{^{1}H\}$ NMR spectra of **5a** in D_2O taken immediately after preparation of the solution (top) and in 24 h (bottom).

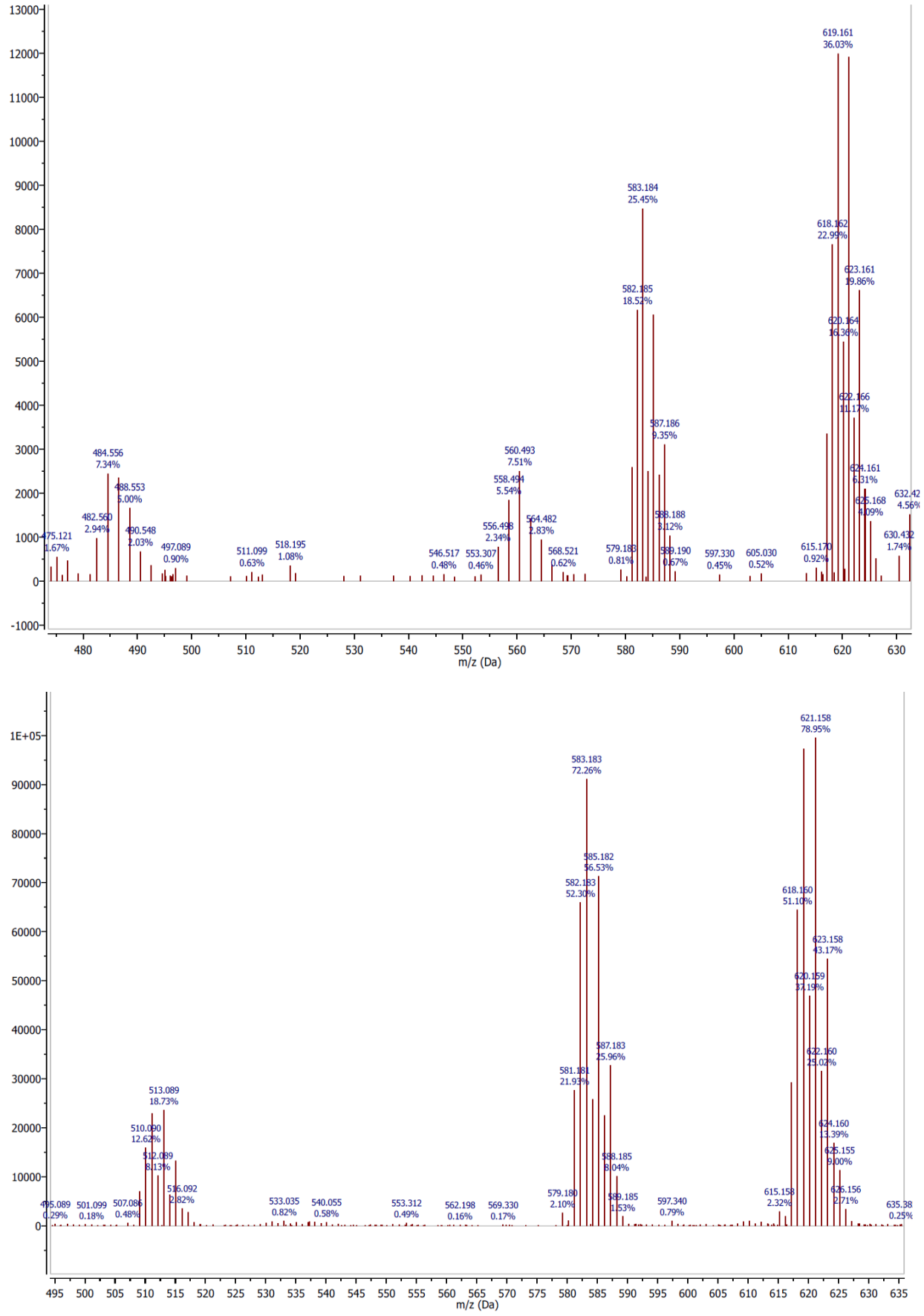

Figure S6. HR ESI^{+}-MS spectra of **4a** in 5 mM NaCl taken immediately after preparation of the solution (top) and in 24 h (bottom).

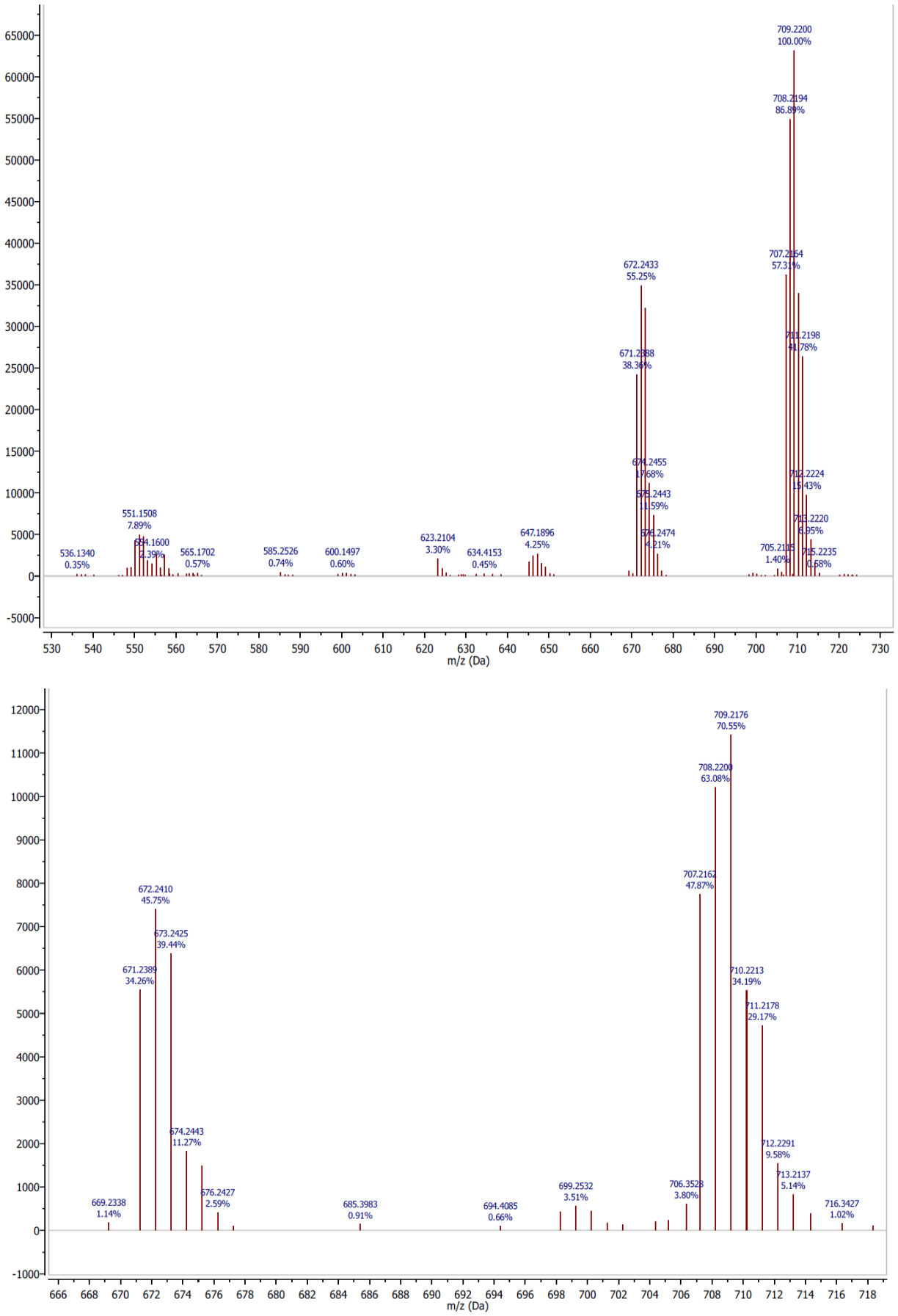

Figure S7. HR ESI$^+$-MS spectra of **5a** in 5 mM NaCl taken immediately after preparation of the solution (top) and in 24 h (bottom).

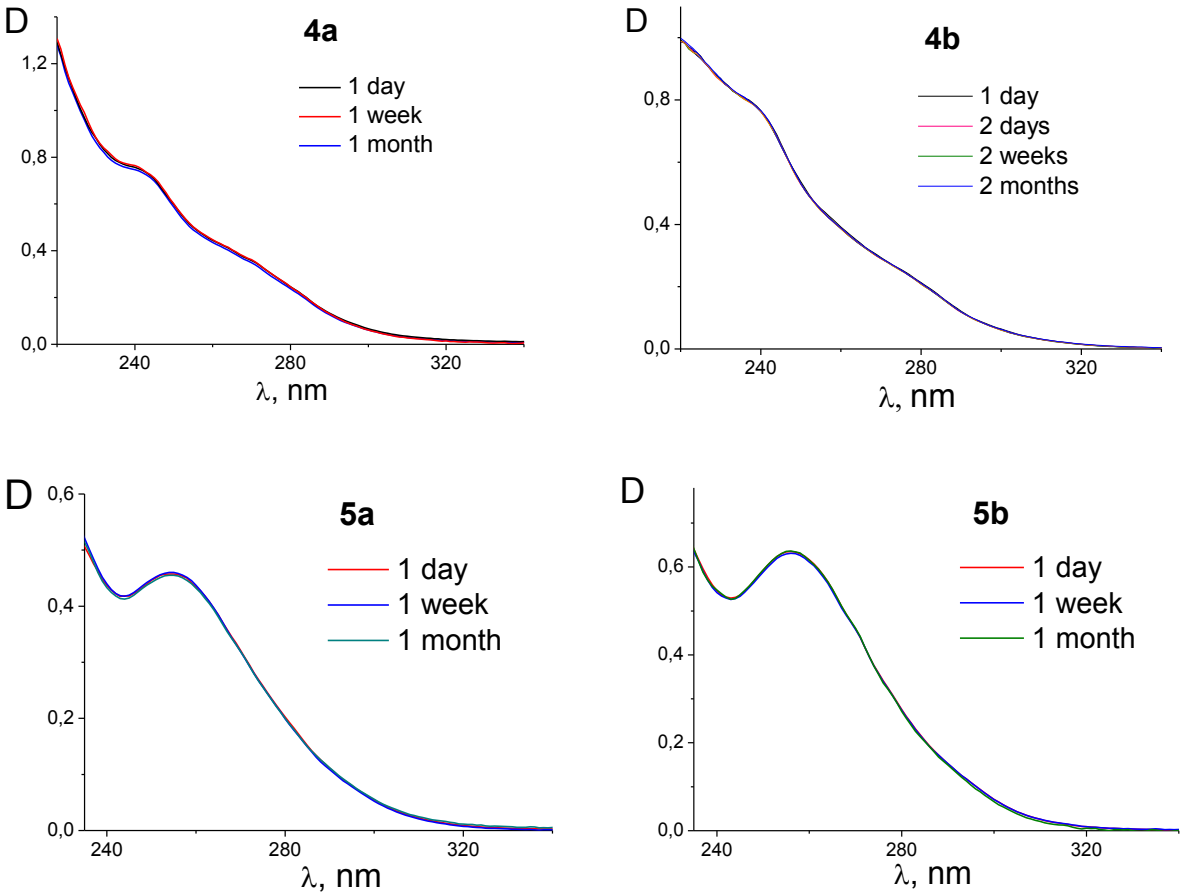

Figure S8. UV absorption spectra of ADC complexes **4a,b** and **5a,b** in 5 mM NaCl taken 1day, 1 week and 1 month after preparation of the solutions.

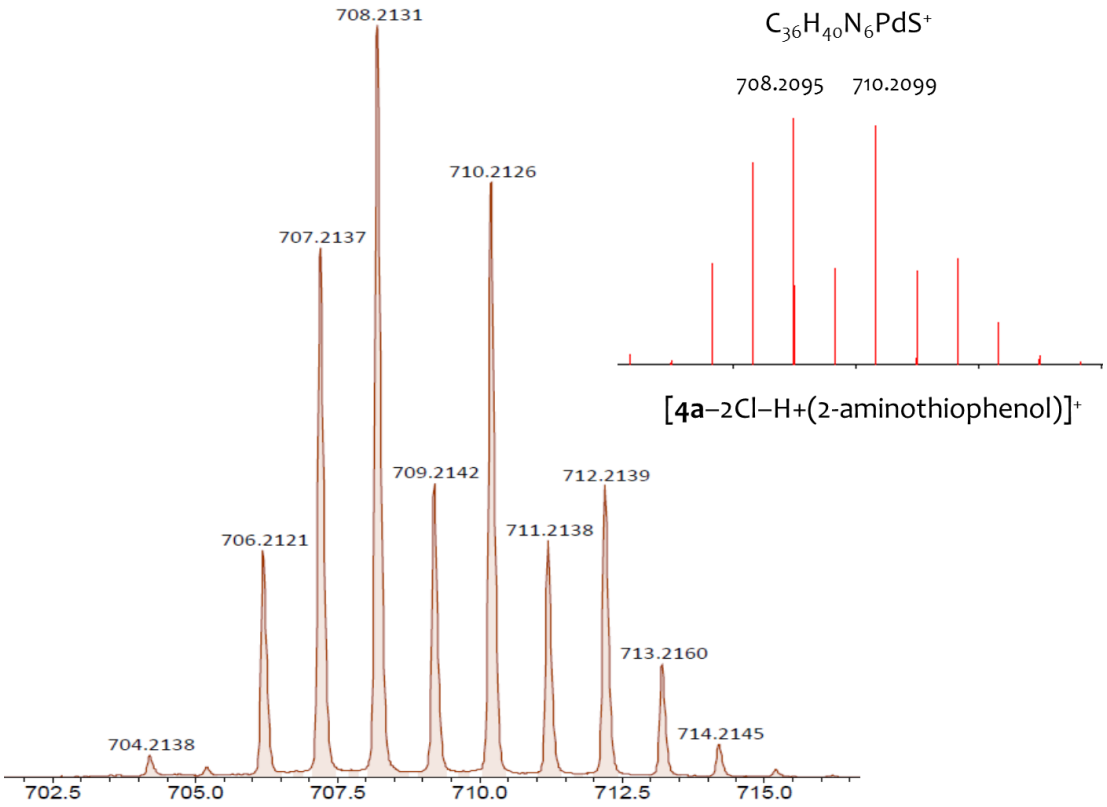

Figure S9. HR ESI$^+$-MS spectra of **4a** in MeOH after addition of equimolar amount of 2-aminothiophenol.

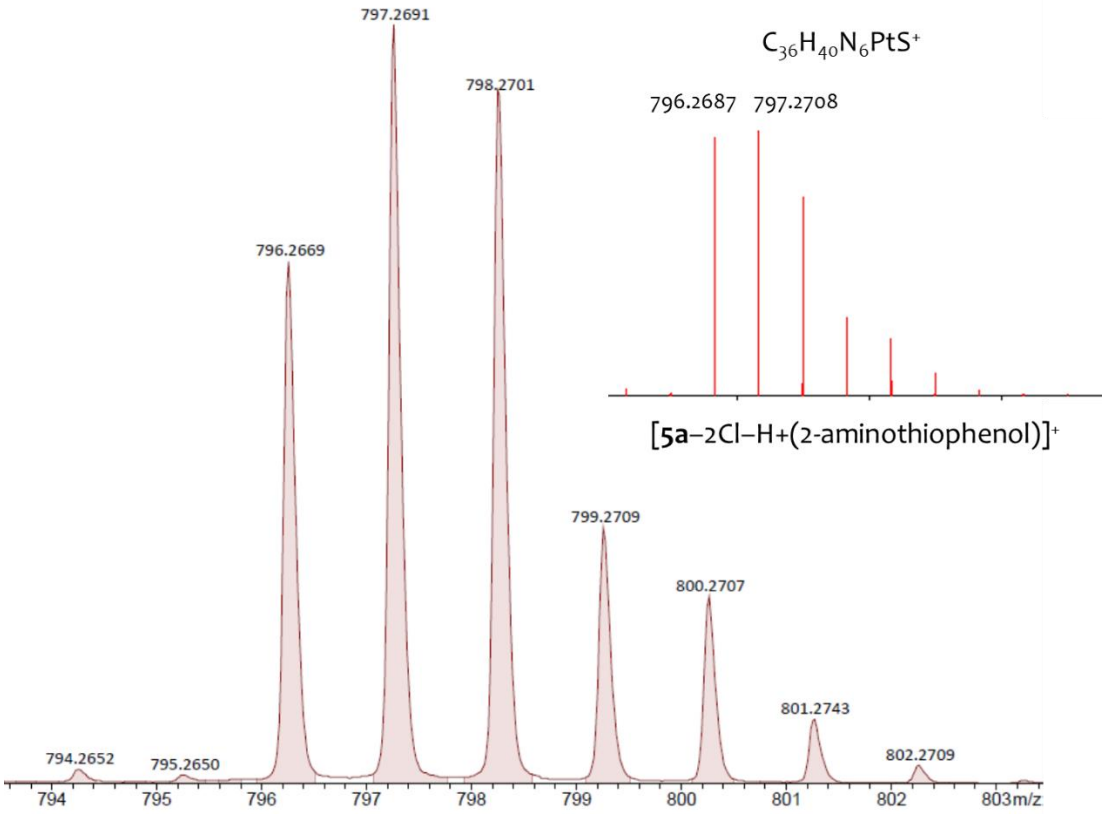

Figure S10. HR ESI$^+$-MS spectra of **5a** in MeOH after addition of equimolar amount of 2-aminothiophenol.

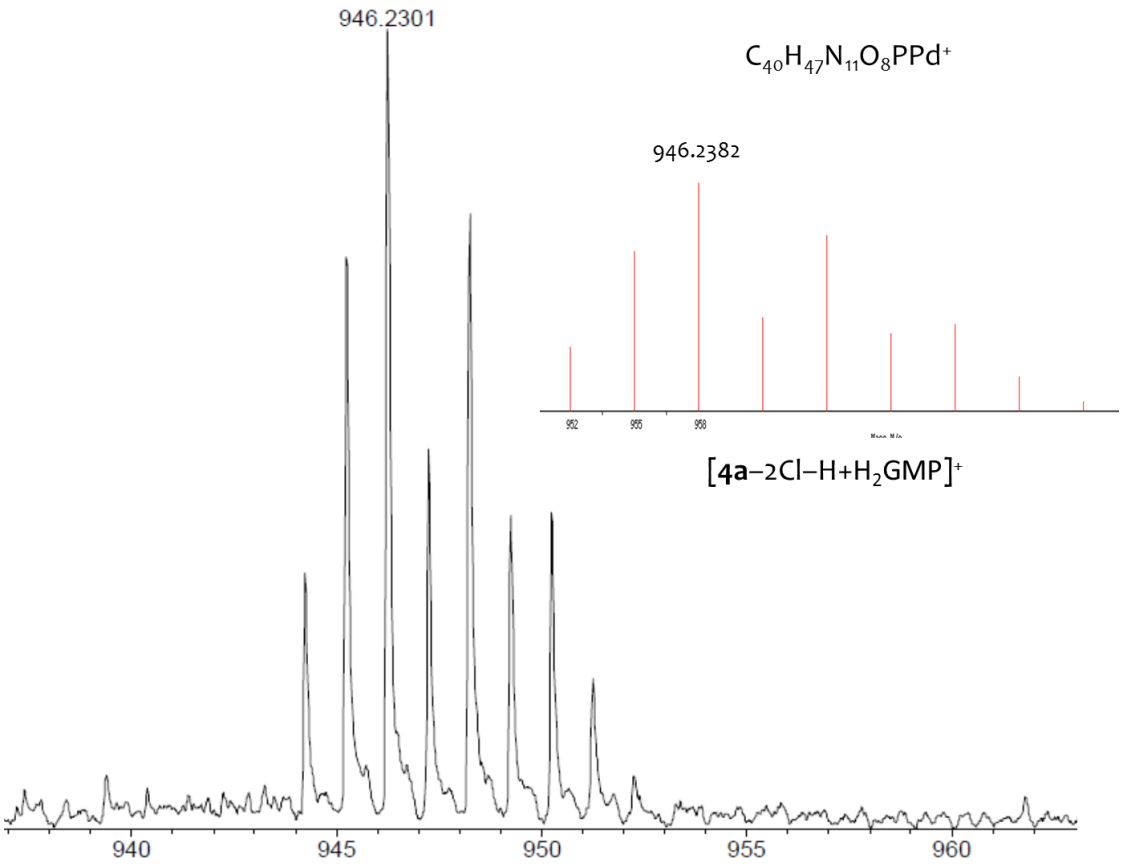

Figure S11. HR ESI$^+$-MS spectra of **4a** in MeOH after addition of equimolar amount of guanosine 5′-monophosphate disodium salt (Na_2GMP).

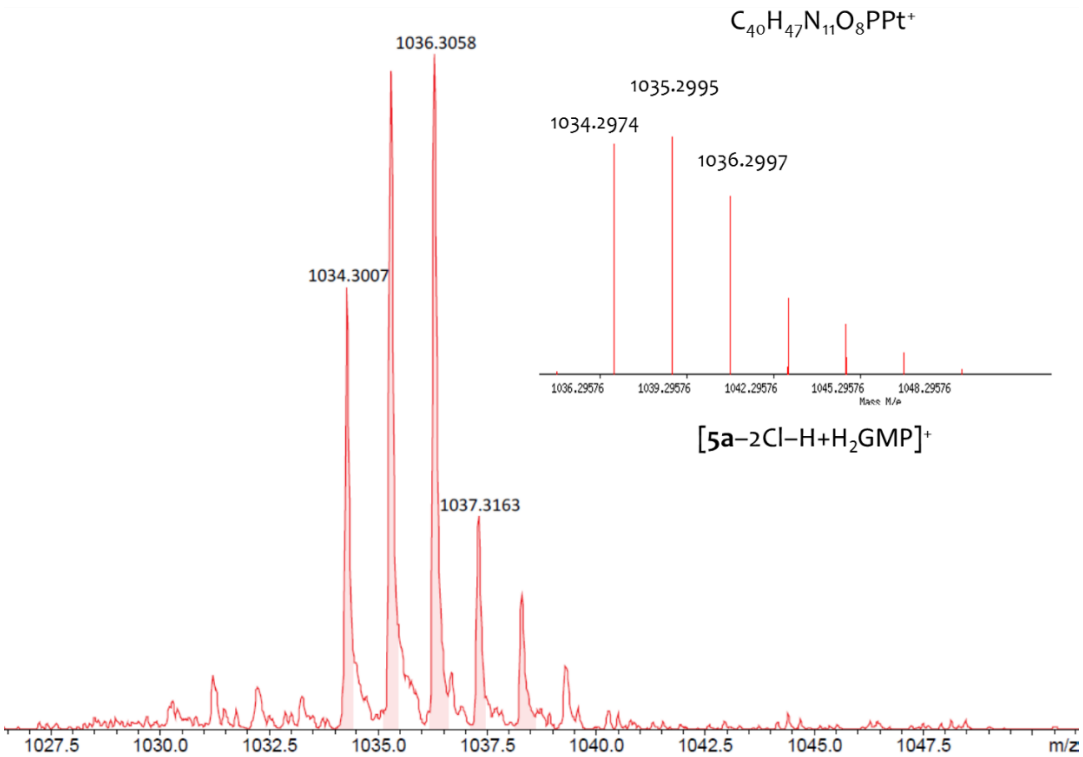

Figure S12. HR ESI$^+$-MS spectra of **5a** in MeOH after addition of equimolar amount of guanosine 5′-monophosphate disodium salt (Na_2GMP).

S5. DNA binding studies

A. UV absorption

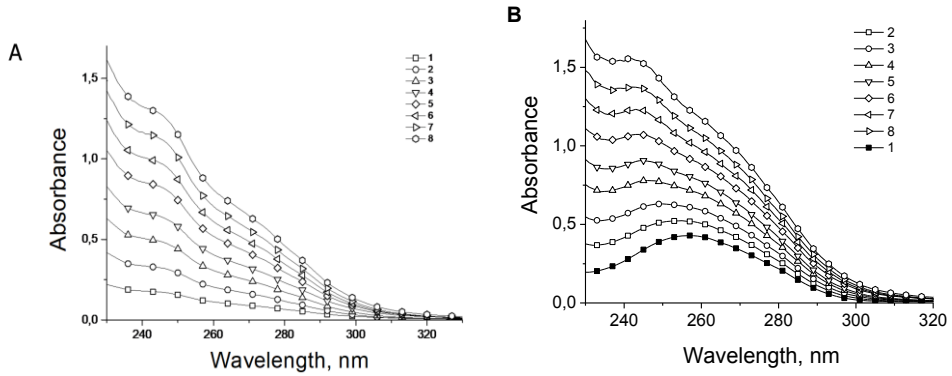

Figure S13. Absorption spectra of **4a** in 0.005 M NaCl (**A**), C(4a)x10^5M = 0.6 (1), 1.2 (2), 1.8 (3), 2.4 (4), 3 (5), 3.6 (6), 4.2 (7), 4.8 (8) ; and DNA-**4a** adducts in 0.005 M NaCl (**B**), r(bp) = 0 (1), 0.2 (2), 0.4 (3), 0.6 (4), 0.8 (5), 1 (6), 1.2 (7), 1.4 (8).

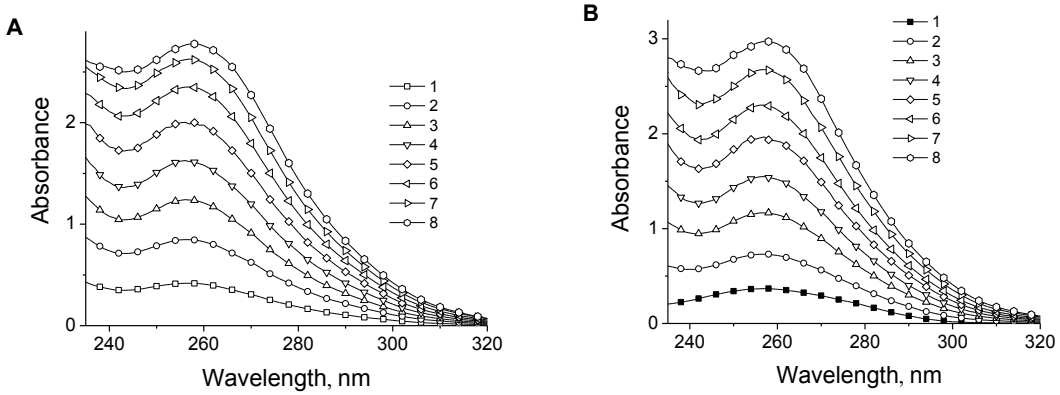

Figure S14. Absorption spectra of **5a** in 0.005 M NaCl (**A**), C(**5a**)x10^5 M = 0.5 (1), 1 (2), 1.5 (3), 2 (4), 2.5 (5), 3 (6), 3.5 (7), 4 (8); and DNA-**5a** adducts in 0.005 M NaCl (**B**), r= 0 (1), 0.2 (2), 0.4 (3), 0.6 (4), 0.8 (5), 1 (6), 1.2 (7), 1.4 (8).

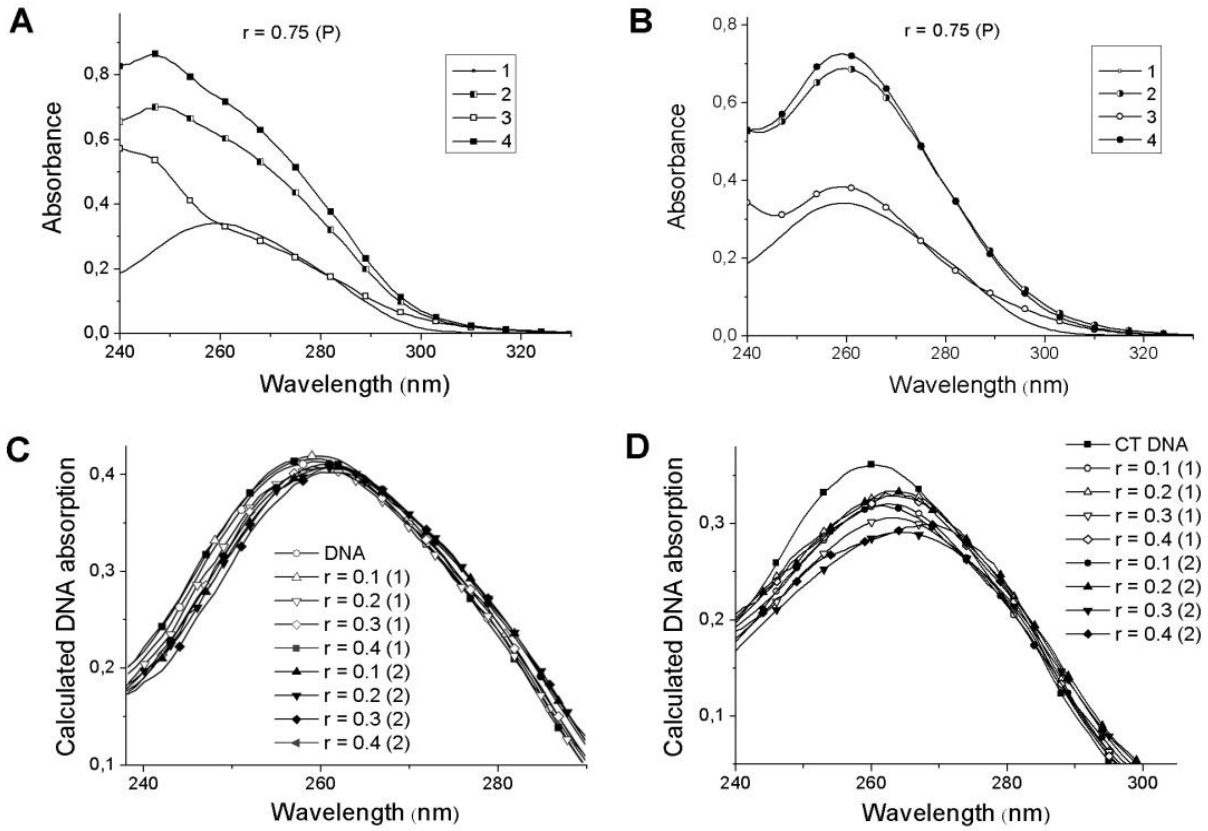

Figure S15. Spectral changes as a result of ADC binding to CT DNA at r = 0.75 for **4a** (A) and **5a** (B): absorption spectra of DNA (1), ADC compound (2), DNA-ADC adducts (3) and a sum of DNA and ADC compound spectra (4); calculated spectra of CT DNA upon titration with **4a** (C) and **5a** (D) after the mixing of the DNA and ADC solutions (1), and in 24 h (2).

B. DNA protonation study

To specify the site of the ADC complexes coordination to DNA, the following DNA protonation experiment was performed. Upon acidification of DNA solution below pK_a value, DNA protonation at guanine N7 atoms takes place (pK_a = 4.75 in 0.005 M NaCl). The first step of protonation occurs without destruction of the DNA double-stranded structure and is accompanied by a hypochromic effect and a small bathochromic shift of the DNA absorption maximum (see Fig. S12 in ESI).[26] Similar changes are observed for ADC-DNA adducts at neutral pH. This makes it difficult to interpret the spectral data, but the type of the changes indicates that guanine N7 atom is suitable for protonation in DNA solution with ADC adducts. Therefore, viscometry was utilized as the main method to monitor DNA protonation in the presence of ADC compounds. For the experiment, high concentrations of DNA (1.8×10^{-4} M nucleotides) and low concentrations of ADC compounds (7×10^{-6} M or 8 ADC molecules per 100 DNA base pairs) were used to minimize formation of intermolecular contacts. Thus, only a small number of binding sites were filled by complexes **4a** or **5a**, providing a possibility for DNA protonation.

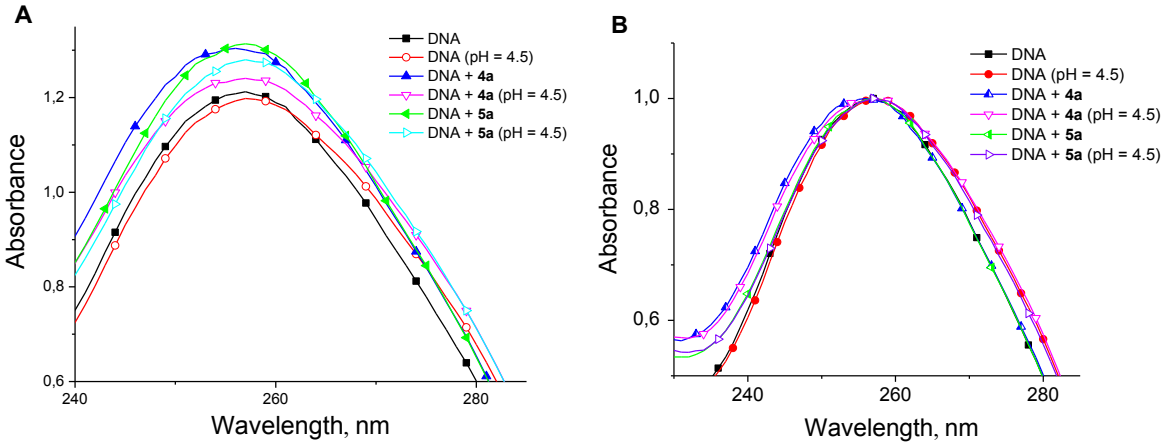

Figure S16. Absorption (**A**) and normalized (**B**) spectra of CT DNA in absence and in the presence of ADC complexes **4a** and **5a** at different pH values.

The obtained viscometric data (**Table S4**) show that, in the absence of the ADC compounds, DNA protonation (the appearance of positive charges on a negatively charged DNA) decreases the solution viscosity due to DNA shrinkage. On the contrary, ADC binding to DNA at neutral pH leads to a great increase in solution viscosity. Moreover, at pH values below pK_a, viscosity of solutions with ADC-DNA adducts decreases less than viscosity of the blank DNA solution (in the case of **4a**) or remains virtually unchanged (in the case of **5a**). This result unambiguously indicates that guanine N7 atoms are involved into formation of coordination bonds with ADC compounds **4a** and **5a** (the binding prevents DNA protonation).

Table S4. Reduced viscosity of DNA solutions (in dl/g) in 0.005 M NaCl before and after its binding with compounds **4a** and **5a**

pH	7.5	5.5	4.5	Relative change in reduced viscosity at pH=4.5 and pH=5.5
DNA	86 ± 1	85 ± 1	58± 1	0.68
DNA + **4a**		111± 2	87± 1	0.78
DNA + **5a**		93± 2	89± 2	0.96

C. CD spectroscopy

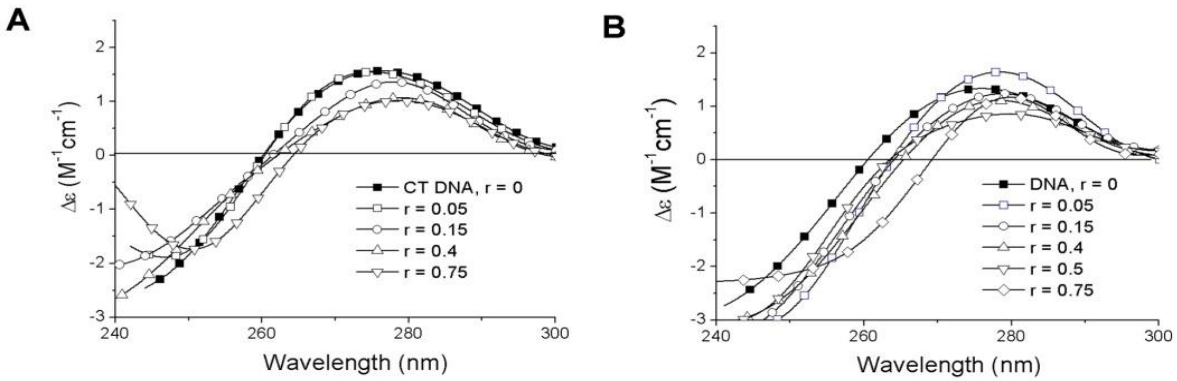

Figure S17. CD spectra of CT DNA upon interaction with **4a** (**A**) and **5a** (**B**) registered in 24 h after mixing the solutions.

D. AFM imaging

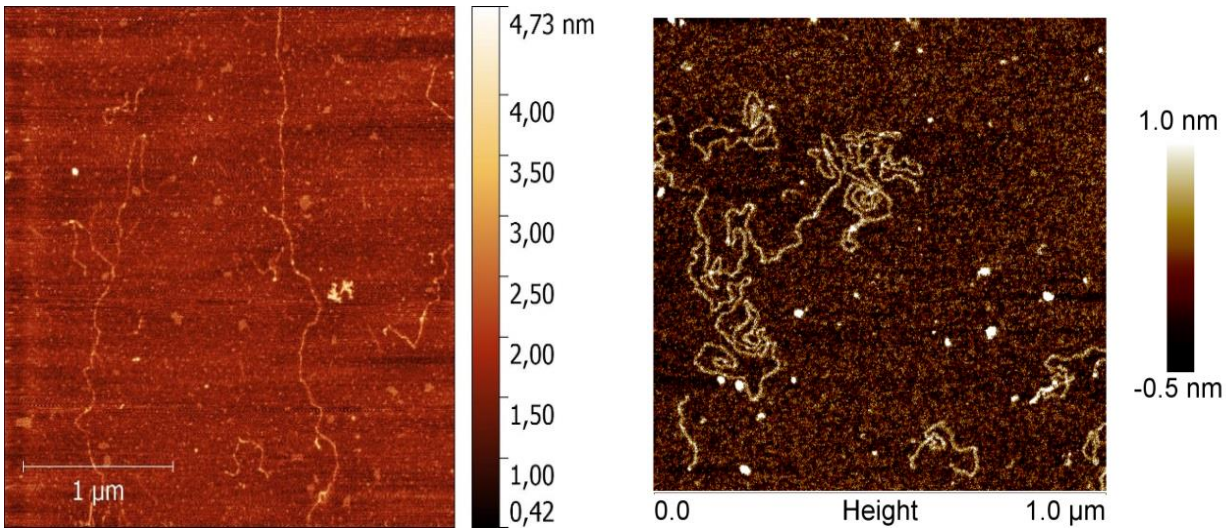

Figure S18. AFM images of DNA (left) and DNA-*cis*-DDP adduct (right). DNA was fixed on mica surface from solutions with C(DNA) = 0,0005%, C(*cis*-DDP) =$5 \cdot 10^{-5}$ M.

E. Hydrodynamic methods

To estimate the effect of the ADC complexes binding on the DNA tertiary structure, hydrodynamic methods including viscometry and flow birefringence were applied. It is known that the dependence of DNA intrinsic viscosity on the concentration of biologically active agent can reflect the change in a volume of DNA molecular coil upon interaction and, therefore, can be used to discriminate different modes of DNA binding.[27] However, in the case of strong ligand-DNA binding, it is also possible to consider the changes of reduced viscosity at a fixed DNA concentration. For example, upon binding with *cis*-DDP, both DNA intrinsic viscosity and reduced viscosity of DNA solutions decrease even at low concentrations of the drug in DNA solution, while the optical anisotropy of DNA statistical segment does not change at low *cis*-DDP concentrations and decreases at $r > 0.4$.[26, 28]

By contrast to DNA complexes with *cis*-DDP, interaction of CT DNA with compounds **4a** or **5a** is accompanied by a significant increase in reduced viscosity of the DNA solutions (Fig. 10). This effect is more pronounced for **4a**, especially on the second day of the experiment. Moreover, compound **4a** induces an increase in reduced viscosity of the DNA solution at lower concentrations than **5a**. The observed increase of reduced viscosity cannot be attributed to coordination mode of binding. Furthermore, the observed huge increase in reduced viscosity of CT DNA solutions upon interaction with the ADC complexes cannot be explained by intercalation due to the principle of an excluded neighbor for the intercalation mode.[29]

The rise of a solution viscosity might be caused by an increase in DNA rigidity (or DNA persistent length). In this case, more than twofold increase in DNA persistent length would be required to explain a huge growth of reduced viscosity observed experimentally (see equation 1 in ESI). However, the measured optical anisotropy of DNA statistical segment ($\alpha_1 - \alpha_2$) does not change upon binding with **4a** and only slightly decreases in the solutions with **5a** (Fig. 10). It is known that optical anisotropy of base pair $\Delta\beta$ for B-form DNA has a maximal value due to the close to normal orientation of base pairs to the axis of the double helix.[30] The invariance or small changes in (α_1-α_2) values show that DNA persistent length does not change significantly upon adduct formation.

Finally, the observed increase in reduced viscosity may be caused by the formation of intermolecular structures due to the simultaneous binding of one ADC compound to the different DNA molecules at the concentrations used (2×10^{-4} M nucleotides for DNA and $> 10^{-5}$ M for **4a** or **5a)**. In order to verify this assumption, additional AFM experiments were carried out. As shown in Fig. 9, AFM images confirmed the appearance of intermolecular contacts along with thickening of the filaments.

To elucidate the nature of the observed contacts, we additionally measured reduced viscosity of CT DNA solutions in the presence of the ADC compounds in 1 M NaCl. In this case, a significant instability of solutions (large variation of the measured viscosity values) was observed in contrast to the measurements carried out in 0.005 M NaCl. Nonetheless, in 1 M NaCl we still observed an increase in viscosity of the DNA solutions with the addition of **4a** and **5a** (see Fig. S15). Unchanged absorption spectra of the components after their mixing in 1 M NaCl (see Fig. S16) indicate that, under these conditions, the ADC compounds **4a** and **5a** do not interact with DNA nitrogen bases. Besides, an excess of salt interferes with electrostatic interactions, which can favor additional contacts **4a** and **5a** with DNA in 0.005 M NaCl. Therefore, to explain an increase of reduced viscosity of DNA solutions in 1 M NaCl, we have to consider some type of interaction that does not affect either DNA or ADC chromophores, but may contribute to the formation of

intermolecular contacts. For example, it may be external binding of the ADC compounds to the DNA double helix realized *via* hydrophobic interactions of the aromatic moieties of the ADC compounds. Additionally, the formation of hydrogen bonds between amino moieties of the ADC compounds and DNA phosphates might be involved.

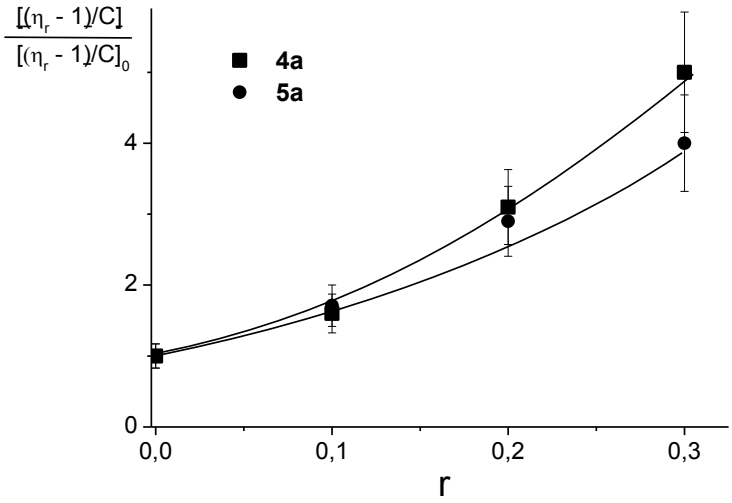

Figure S19. Dependence of the relative change in reduced viscosity of DNA solutions on r value in 1 M NaCl for ADC compounds **4a** and **5a**.

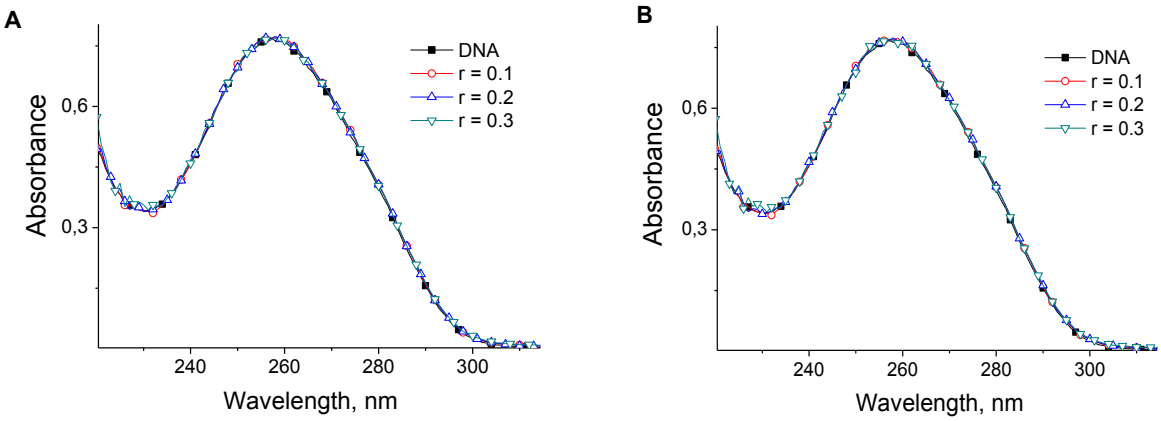

Figure S20. Calculated DNA absorption spectra in the presence of **4a** (A) and **5a** (B) in 1 M NaCl solutions taken in 24 h after mixing the solutions.

F. Competitive fluorescence study with DAPI

Fluorescence quenching is known as a sensitive technique commonly used to determine the localization of new drugs and their mode of interaction with DNA [31]. EtBr, Hoechst 33258 and other fluorescent dyes, the emission of which is enhanced upon binding to dsDNA, are frequently utilized for competitive binding studies with new metallodrugs [27]. In the present study, we used 4′,6-diamidino-2-phenylindole (DAPI), a fluorescent dye that interact with dsDNA *via* a combination of minor groove binding with electrostatic attraction to DNA phosphates [32-34].

It is known that DAPI interaction with DNA leads to a significant enhancement of the dye fluorescence intensity. DAPI fluorescent spectra reveal two modes of its binding to DNA. At low z values ($z < 0.05$, z is the ratio of molar concentrations of DAPI and DNA phosphates), dye molecules are localized mainly in a minor groove of DNA with partial intercalation between nitrogen bases and formation of hydrogen bonds. This strong mode of DAPI binding is manifested in luminescence with a high quantum yield with maximum at 440 nm and excitation at 340 nm (at the maximum of DAPI absorption band). At higher DAPI concentrations ($z > 0.05$), the second weak mode of DAPI electrostatic binding to DNA phosphates can be observed. This interaction is manifested through lower luminescence with maximum at 540 nm and excitation at 420 nm. Earlier [32], we demonstrated that both types of DAPI interaction with dsDNA can be detected in solution at $z = \text{DAPI/DNA} \approx 0.3$.

For the competitive binding experiment, DAPI luminescent spectra were registered in 24 h after the addition of DAPI to the solutions with DNA-ADC adducts. As can be inferred from Fig. S17, DNA adducts with complexes **4a** and **5a** have similar impact on DAPI luminescence. The shape and intensity of DAPI emission spectra in complexes with DNA depend on the concentration of ADC complexes (or r value). At $r < 0.3$ the binding of ADC compounds to DNA does not affect significantly DAPI luminescence. At $r > 0.3$ one can observe changes in DAPI luminescence. Namely, an increase in intensity of emission at 440 nm (λ_{ex} = 340 nm) indicates that the contribution of DAPI minor groove binding rises with growth of **4a** and **5a** concentration in solution (Fig. 9B). On the contrary, the electrostatic binding of DAPI to DNA phosphates weakens (as one can see from the decrease in the emission at 540 nm and λ_{ex} = 420 nm). It should be noted that similar changes in DAPI luminescence are observed in the case of its interaction with DNA bound to *cis*- and *trans*-DDP. *Cis*-DDP has the strongest effect on the DAPI binding in the DNA minor groove, while all other compounds show approximately the same effect. It might be speculated that this is due to the fact that bidentate coordination to DNA is typical for *cis*-DDP [35], whereas monodentate binding is realized for *trans*-DDP [28] and, most probably, prevails in the case of compounds **4a** and **5a**.

Based on the present data, we suggest that **4a** and **5a** bind to DNA nitrogen bases in a major groove, and, probably, this binding transforms a minor groove making it more accessible to DAPI at $r > 0.3$. This effect is more significant in the case of *cis*-DDP. Moreover, weakening of the dye binding to DNA phosphates leads to the release of additional DAPI molecules that may bind DNA in alternative positions. Indeed, the competition between DAPI and the ADC compounds for the phosphate sites is observed at $r > 0.3$. Thus, at $r < 0.3$ DAPI and ADC find possibility to bind separately to DNA (DAPI in a minor groove and ADC in a major groove mainly), whereas at $r > 0.3$ ADC molecules displace the DAPI molecules from the DNA phosphate groups. At any r value, compounds **4a** and **5a** do not bind to DNA in the minor groove.

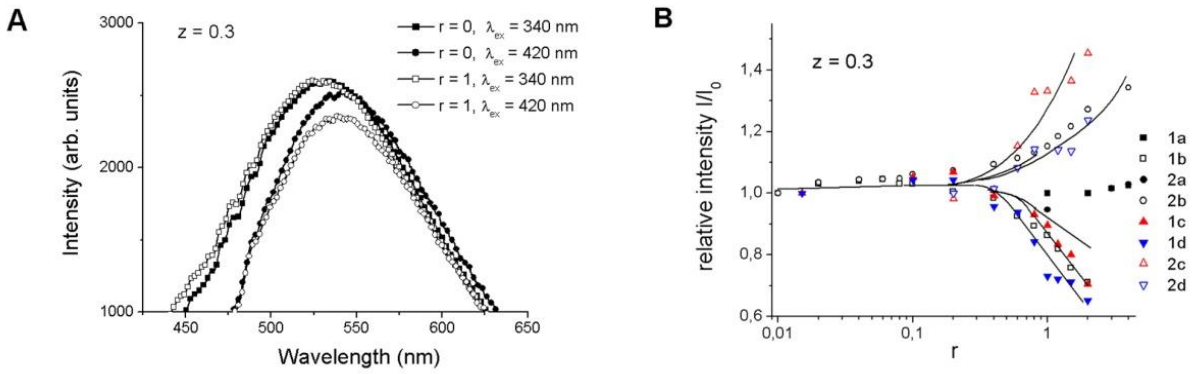

Figure S21. DAPI emission spectra (λ_{ex} = 340 and 420 nm) in DNA solutions in the absence and in the presence of **4a** at r = 1 and z = 0.3 (the spectra at λ_{ex}=420 nm have been multiplied by 12.5) (A); and dependence of relative change in intensity of DAPI luminescence on r value (B) at λ_{em}=540 nm, and λ_{ex}=420 nm (1); at λ_{em}=440 nm and λ_{ex}=340 nm (2) for **4a** (a) and **5a** (b), *cis*-DDP (c) and *trans*-DDP (d); C(DAPI)=5×10^{-6} M = const, C(DNA)=1.5×10^{-5} M (P) = const.

S6. Molecular docking studies

Both **4a** and **5a** share similar structure (all atom RMSD is 0.0304 A), moreover palladium and platinum atoms are sharing similar LJ-potential parameters. As AutoDock 4.2.6 scoring function is based on precomputed grid parameters of defined resolution (0.2 Å spacing for grids of all proteins), compounds **4a** and **5a** would appear totally indistinguishable by scoring function in docking study. So, computation was performed for the structure **4a** alone, considering analogous conformations of **4a** and **5a** in complex with DNA.

As target macromolecules are unchangeable during docking of ligands, different DNA structures were used to test different possible modes of binding of metal-ADC complexes. Dodecameric oligonucleotide d(CpGpCpGpApApTpTpCpGpCpG) (PDB ID 1BNA) was chosen as model for groove binding. As binding of any ligand to DNA could lead to an unpredictable change in geometry of DNA, using stable B-helix structures of DNA is optimal way of estimating binding affinity of tested structures [36]. Still, there is probability of false-positive and false-negative results as DNA structure is prone to change its conformation during binding of any ligand, whereas docking programs like AutoDock are unable of accounting for such conformational changes [14]. Even so, dodecamer 1BNA is often used for docking studies of DNA-targeting molecules to test whether compound under consideration are possible DNA-binders [36, 37].

4a was found to bind 1BNA in AT-reach regions of a minor groove, probably, due to more hydrophobic surrounding inside the groove. As most of **4a** surface is hydrophobic, ligand is prone to locate up to 2 of its aromatic rings inside the groove, leaving the other two outside the cavity. In dicationic form, **4a** can form up to 2 hydrogen bonds with the DNA, whereas monocationic form can create up to 3 hydrogen bonds. This can be related with more rigid structure of dicationic form that makes **4a** harder to fit geometric criteria for creating hydrogen bond and lesser partial negative charges on nitrogen atoms, that weakens hydrogen bonding. **Figures S22** and **S23** show structures of **4a**-lBNA complexes in di- and monocationic form. **Figure S23B** shows overlaid structures of di- and monocationic forms of **4a** in complex with 1BNA indicating similar mode of binding of two forms. Energy of binding of di- and monocationic forms were of -11.8 kcal/mol and -6.5 kcal/mol respectively, indicating dicationic form being stronger binder (mostly due to van der Waals interactions). Still, there is extremely unfavorable interaction of both forms of **4a** with outer media and polar groups of DNA as 2 of aromatic rings of **4a** are situated outside the minor groove.

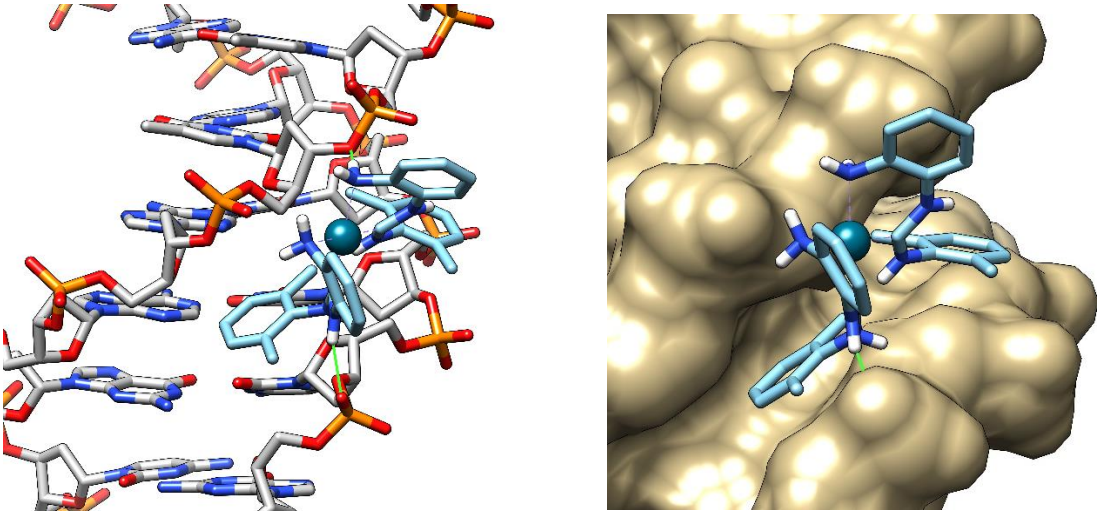

A B

Figure S22. Structure of complex of 1BNA with dicationic form of **4a** with stick (A) and surface (B) representation of 1BNA. Green lines stand for hydrogen bonds between atoms.

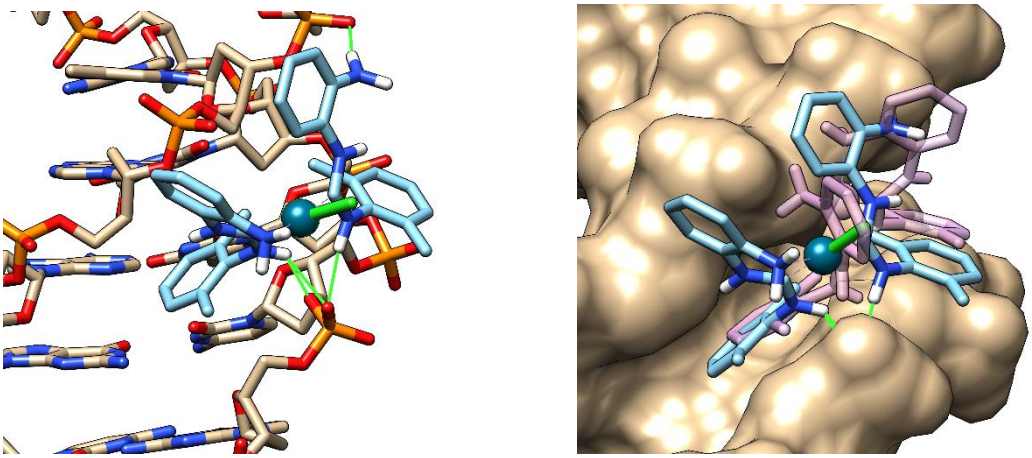

A B

Figure S23. Structure of complex of 1BNA with monocationic form of **4a** with stick (A) and surface (B) representation of 1BNA. Dicationic form of **4a** (pink) is added to the surface representation to visualize differences between binding of two form of **4a** to 1BNA. Green lines stand for hydrogen bonds between atoms.

Octameric oligonucleotide 5′-CCTCG*TCC-3′ (PDB ID 1XRW; asterisk denotes gap between nucleotide pairs formed by intercalated elipticine) was chosen as target structure for intercalation mode of action of **4a**. During preparation of the structure of target protein, intercalated ligand and water molecules were all deleted.

Figure 3 shows result of docking of **4a** as intercalating agent in 1XRW structure. Intercalating of **4a** to DNA molecule have shown little affinity of **4a** forms to 1XRW structure. In both forms, **4a** is only capable of creation of up to 2 hydrogen bonds with surrounding nucleotides. Only one of aromatic rings of **4a** could be situated inside the gap of 1XRW in the same time, because the structure of **4a** could not let them acquire same plane conformation. Di- and monocation forms of **4a** are situated on the different sides of 1XRW, with most of nonpolar surface

located in the outside media and not interacting with DNA. As most of **4a** is not interacting with DNA, di- and monocationic forms of **4a** scored diminutive binding energy with respect to minor groove binding energy: -8,19 kcal/mol for dication and -3.43 kcal/mol for monocation.

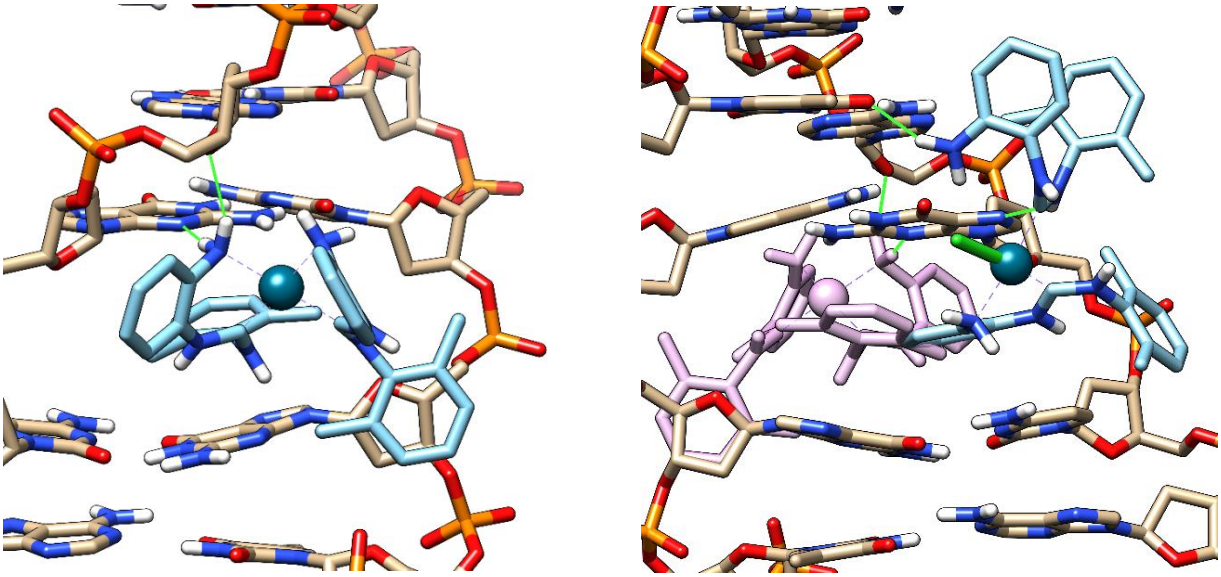

A **B**

Figure S24. Structure of the complexes of 1XRW with dicationic (A) and monocationic (B) forms of **4a**. Dicationic form of **4a** (pink) is added to the structure B to visualize the difference between the binding of the two forms. Green lines stand for hydrogen bonds between atoms.

For the validation of our docking protocol, we have additionally performed a redocking experiment using 1XRW DNA structure as a model. The 1XRW DNA-ligand structure contains platinum-based complex with an acridine moiety that binds to DNA both through intercalation and covalent interaction. The DNA molecule of the 1XRW structure is widely used as a model for an intercalation mode of binding since it bears an intercalation gap that is required for docking study, and, at the same time, the overall conformation of DNA does not undergo any radical changes that could affect resulted conformations.

The redocking studies were performed by the same protocol that was used in the initial study. In every docking run, the acridine moiety of the 1XRW ligand is situated in the gap between nucleobases, while flexible chain bearing metal ion adopts different conformation, as Pt(II) ion is prone to be located near the atoms with high negative charge. Still, most of the times, Pt(II) is situated next to the nucleobase nitrogen atoms. Such complexes correctly represent the binding mode, in which 1XRW ligand interacts with DNA molecule, indicating that our docking protocol is capable of creating correct ligand-DNA complex. Thus, the resulted complexes could be considered as positions of metal complex and DNA that precede formation of a covalent bond between them (if covalent binding occurs).

S7. Antiproliferative activity

Table S5. Antiproliferative activity of compounds **4a**, **5a** and cisplatin as measured by means of MTT assay

Compound	IC_{50} μM				
	SK-OV-3	MCF-7	HT1080	A549	HEK293
4a	46.77±3.62	15.91±1.39	15.36±0.80	60.12±3.55	10.84±0.61
5a	n.d. (74.86)	22.22±0.89	n.d. (27.25)	n.d. (103.7)	17.91±0.87
cis-DDP	10.77±0.63	13.97±1.62	6.89±0.56	21.69±1.40	10.29±1.81

S8. Apoptotic activity

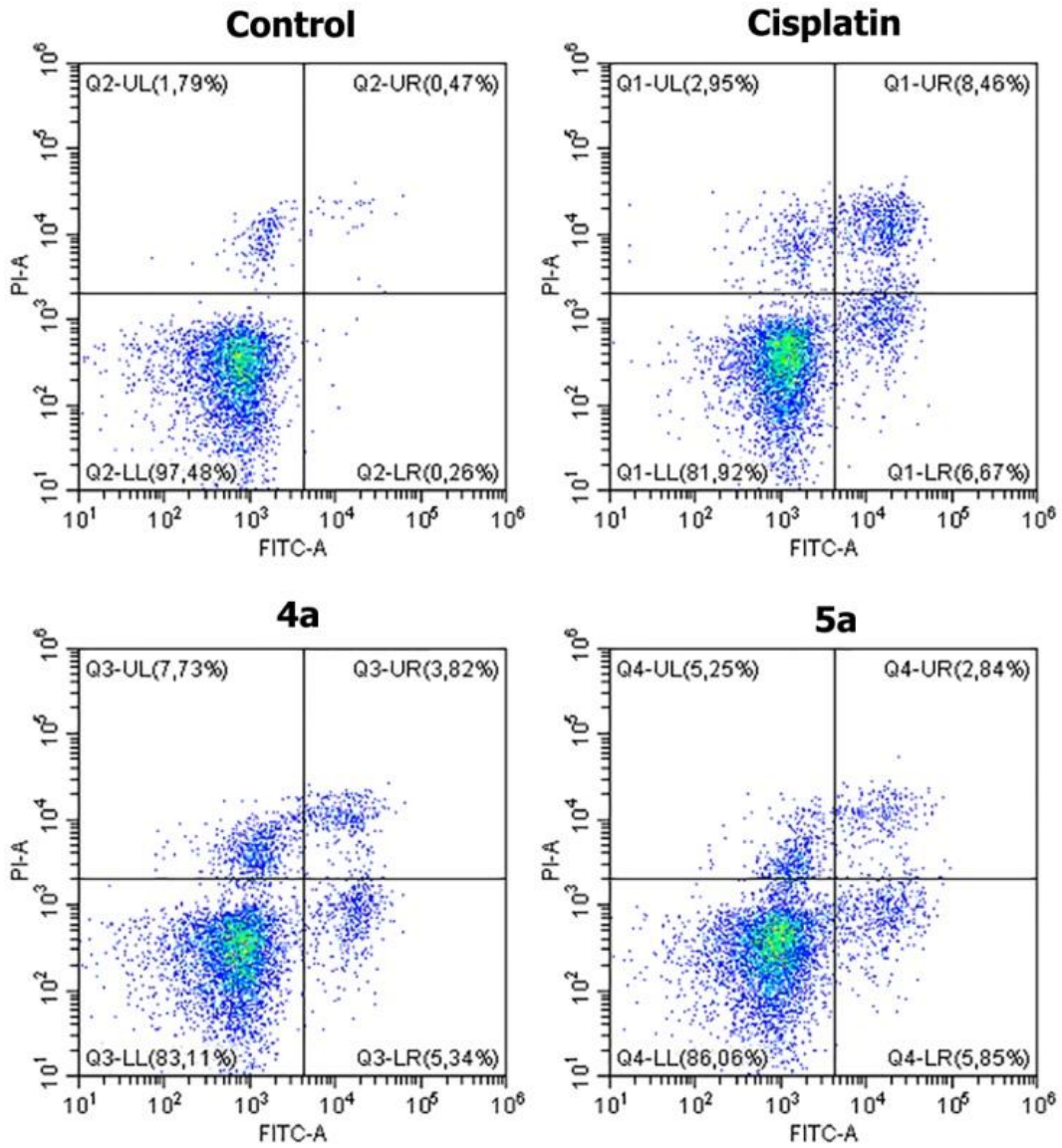

Figure S25. Induction of apoptosis in MCF-7 breast carcinoma cells treated with complexes **4a**, **5a** and cisplatin for 48 h at the concentration of the respective IC_{50} value.

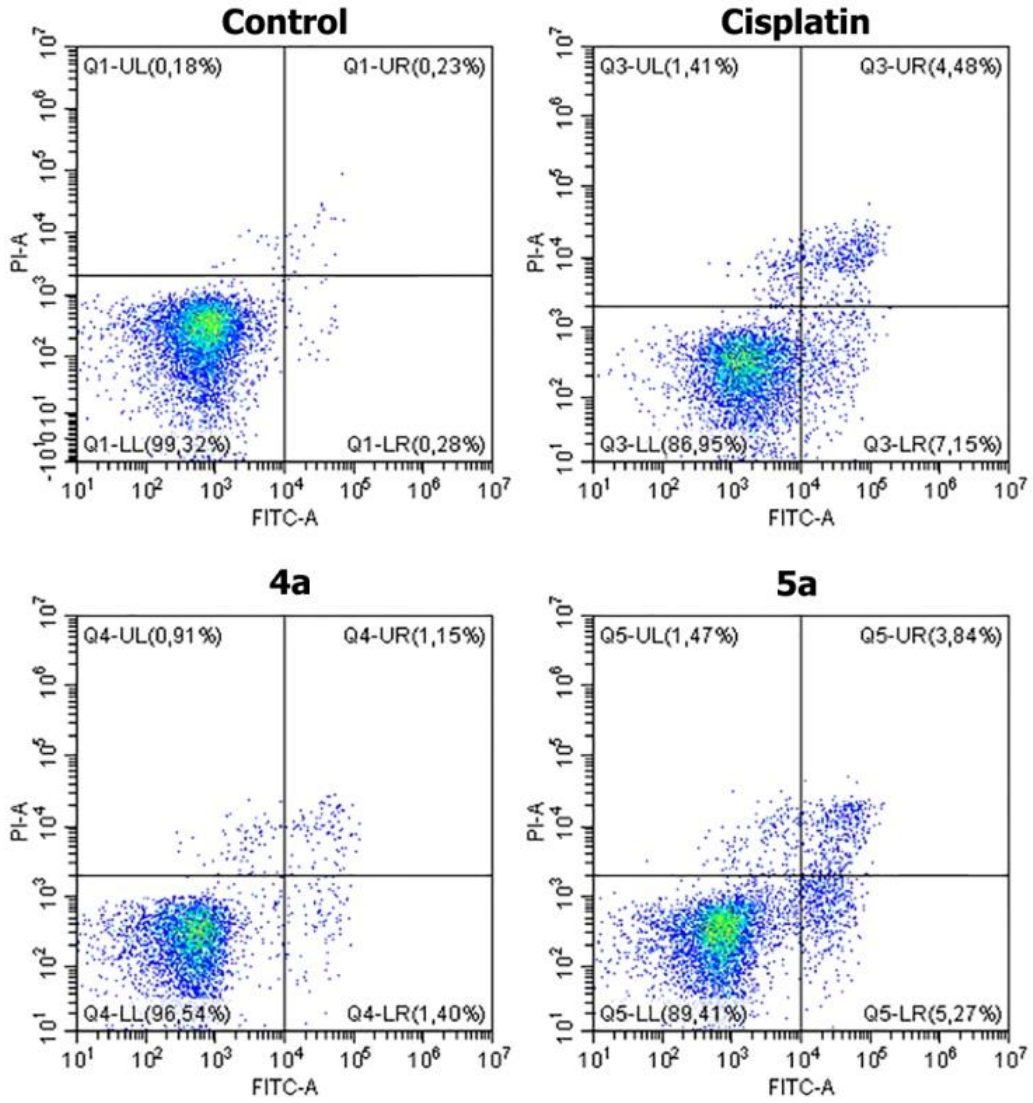

Figure S26. Induction of apoptosis in HT1080 fibrosarcoma cells treated with complexes **4a**, **5a** and cisplatin for 48 h at the concentration of the respective IC_{50} value.

S9. NMR spectra

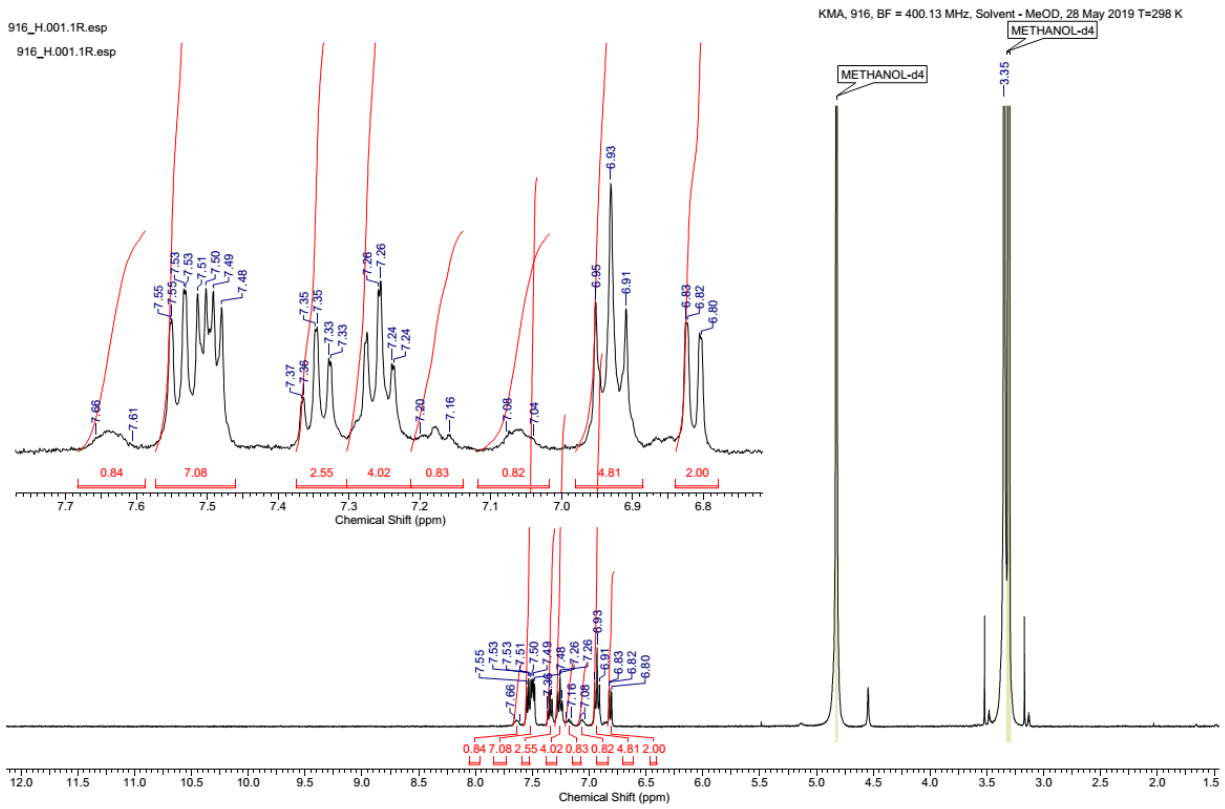

Figure S27. ^{1}H NMR spectrum of **4c** in methanol-*d*4.

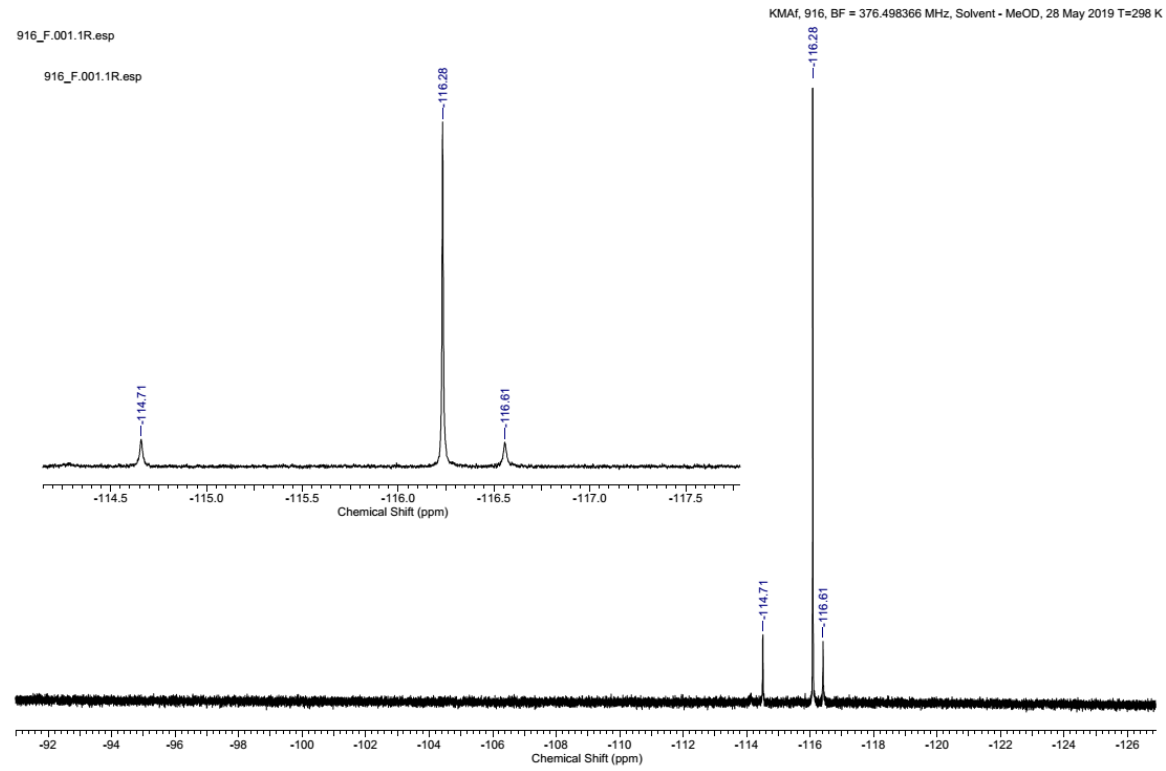

Figure S28. ^{19}F{^{1}H} NMR spectrum of **4c** in methanol-*d*4.

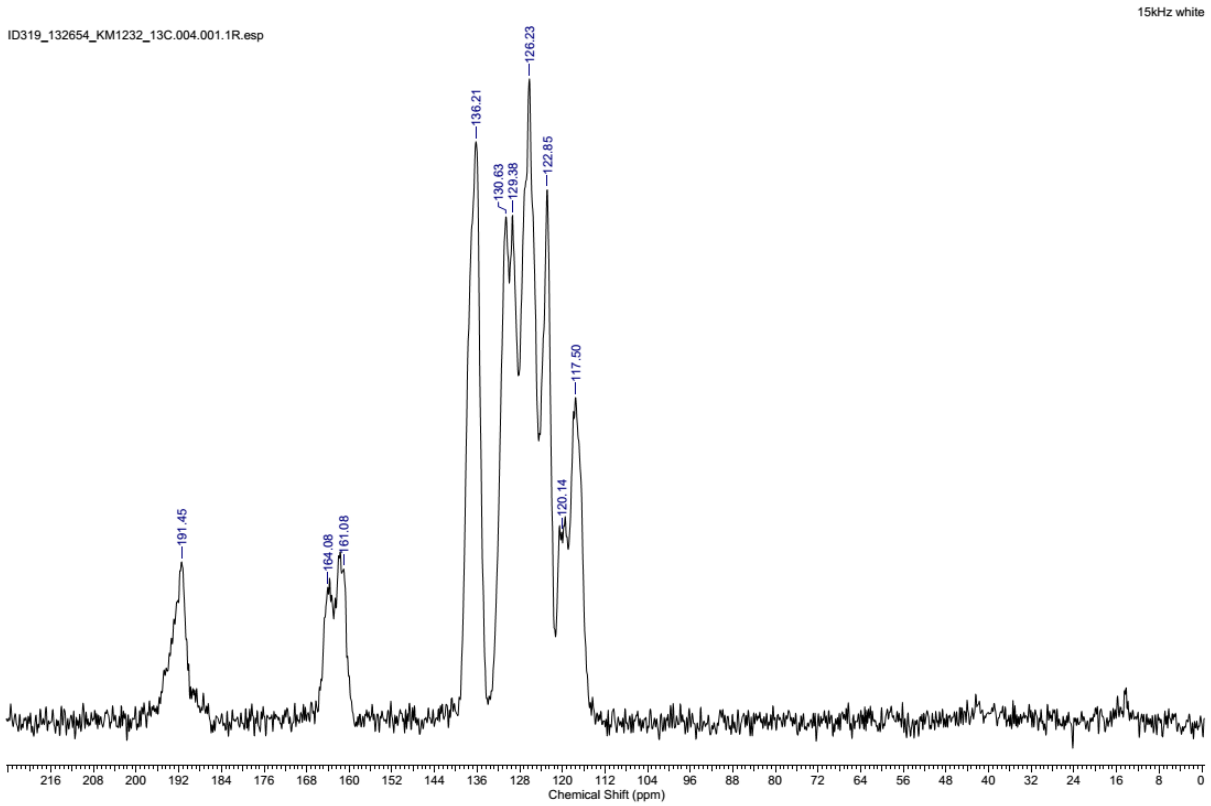

Figure S29. ^{13}C CP/MAS NMR spectrum of **4c** in solid state.

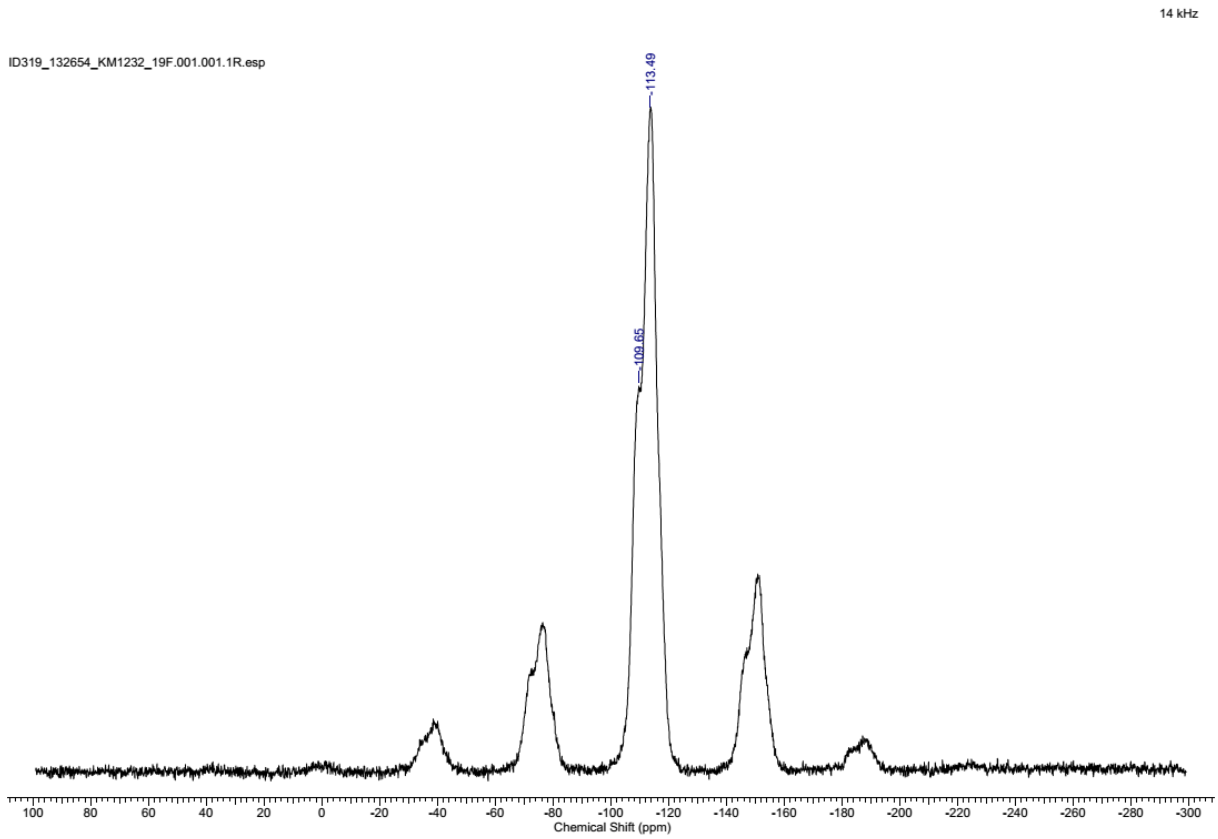

Figure S30. ^{19}F CP/MAS NMR spectrum of **4c** in solid state.

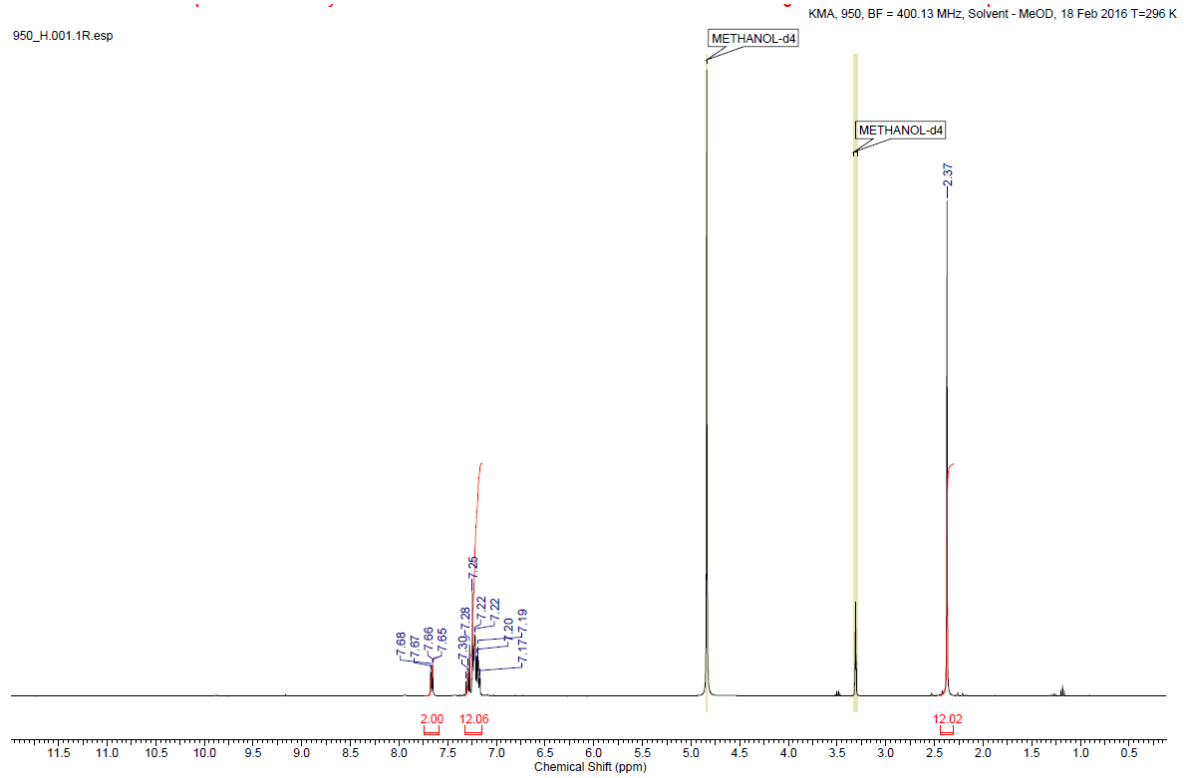

Figure S31. ^{1}H NMR spectrum of **5a** in methanol-*d*4.

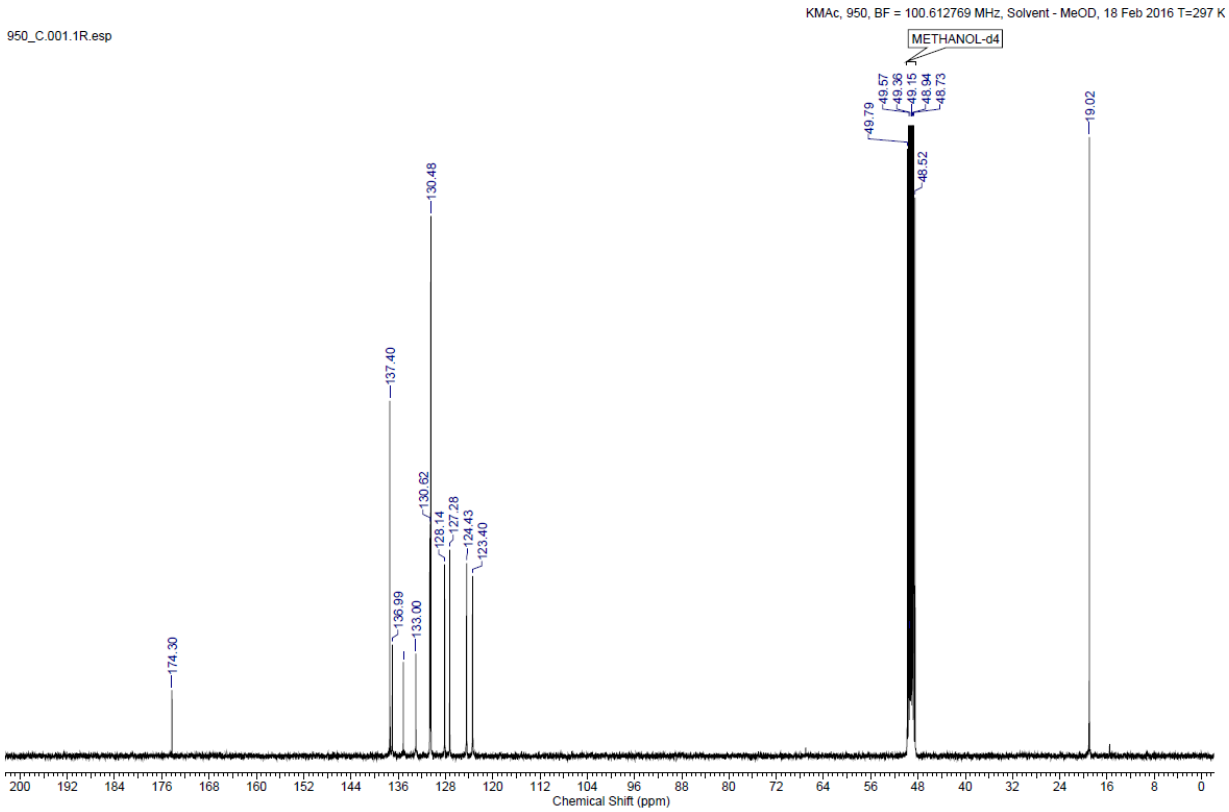

Figure S32. ^{13}C{^{1}H} NMR spectrum of **5a** in methanol-*d*4.

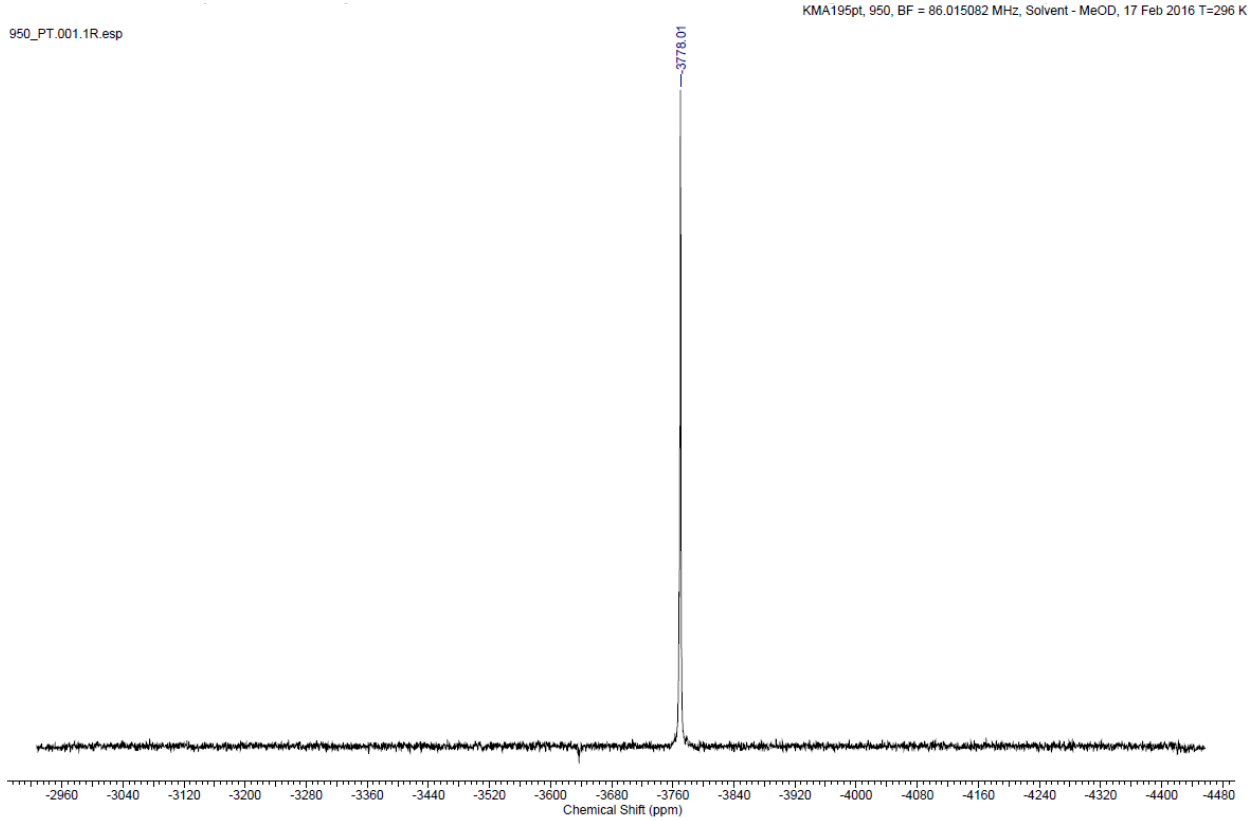

Figure S33. ^{195}Pt{^{1}H} NMR spectrum of **5a** in methanol-*d*4.

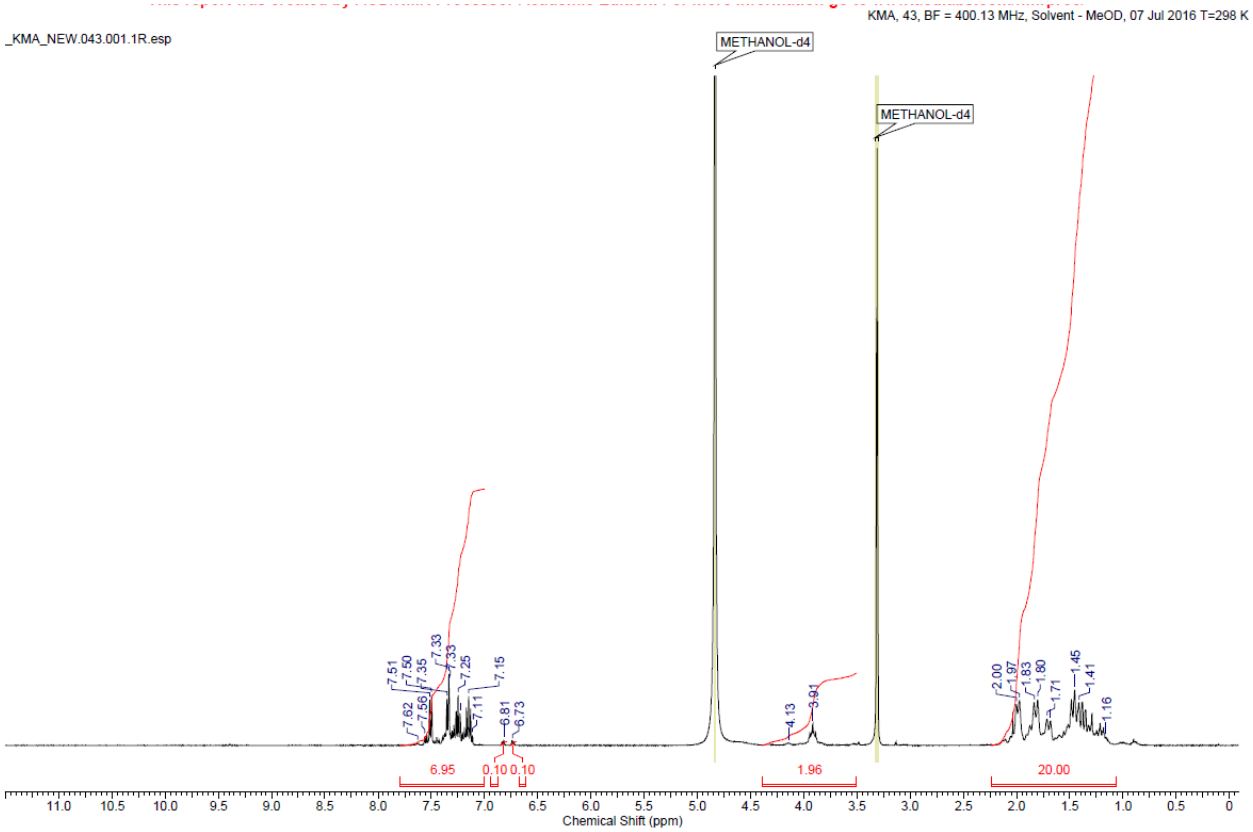

Figure S34. ^{1}H NMR spectrum of **5b** in methanol-*d*4.

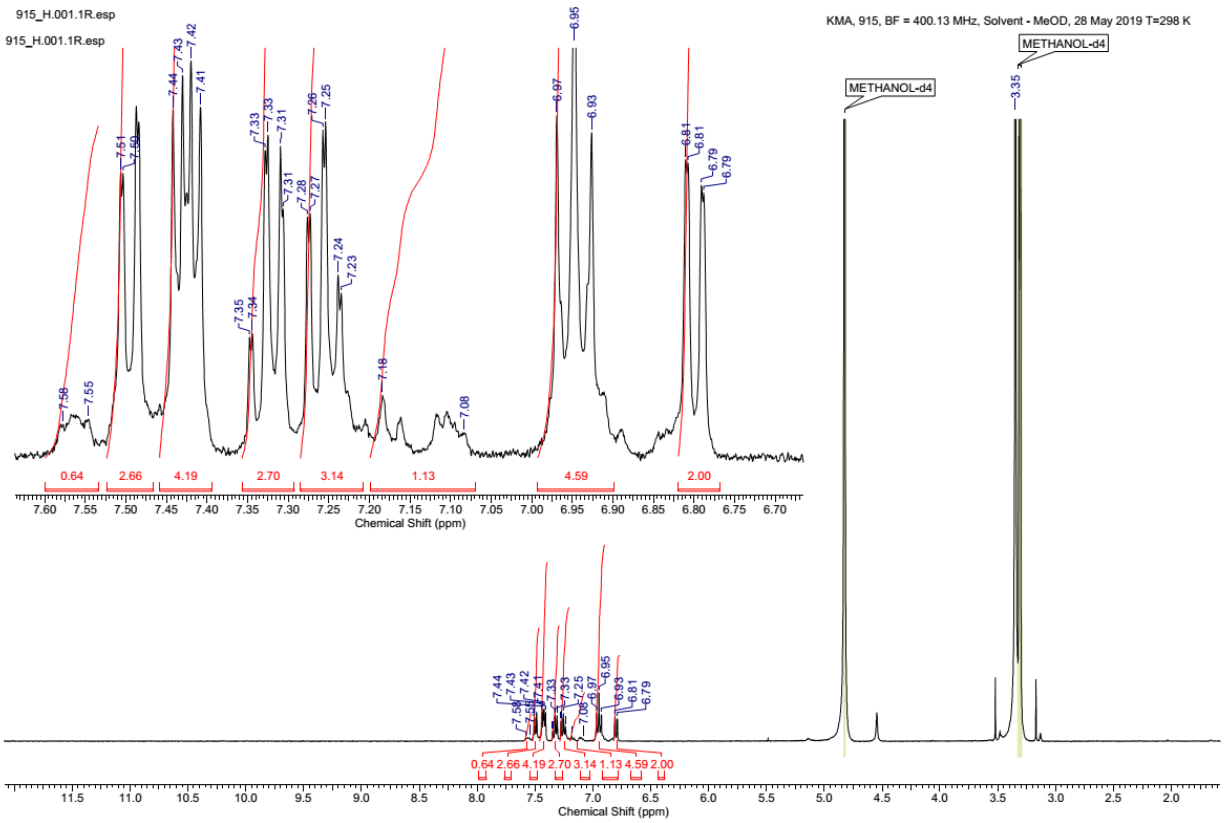

Figure S35. ^{1}H NMR spectrum of **5c** in methanol-*d*4.

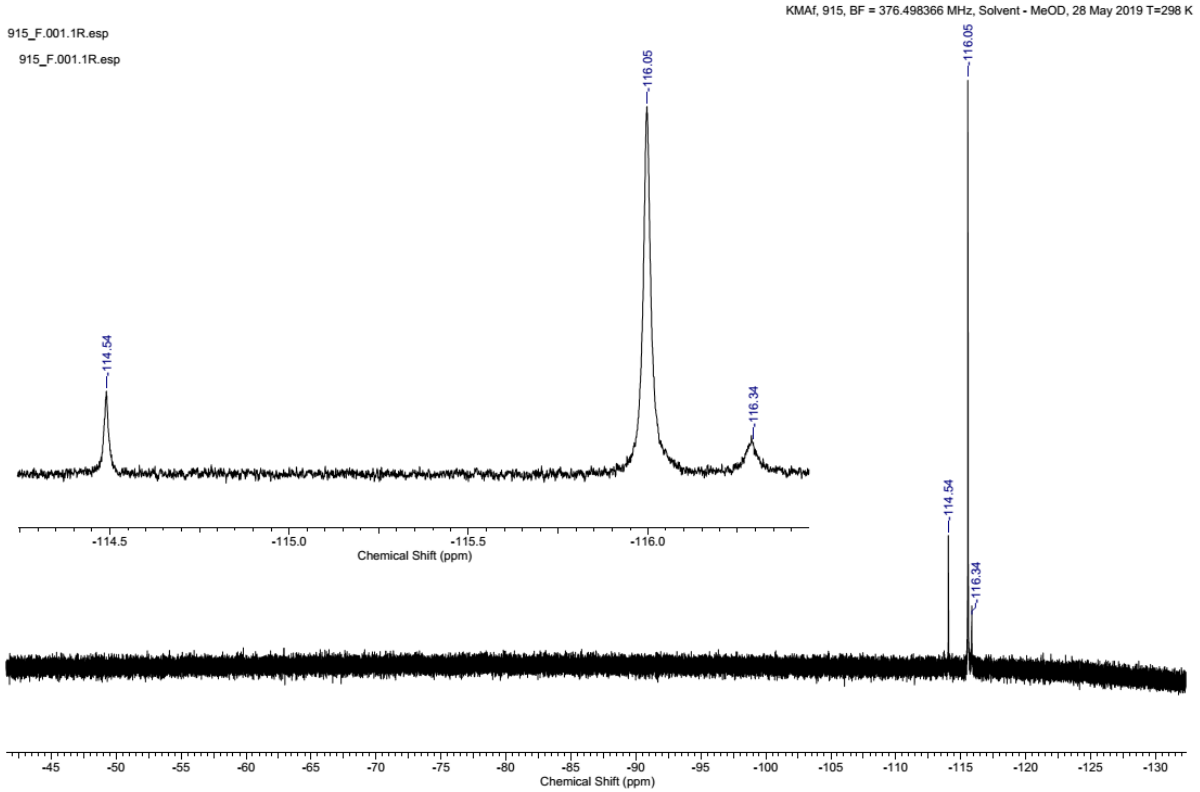

Figure S36. ^{19}F{^{1}H} NMR spectrum of **5c** in methanol-*d*4.

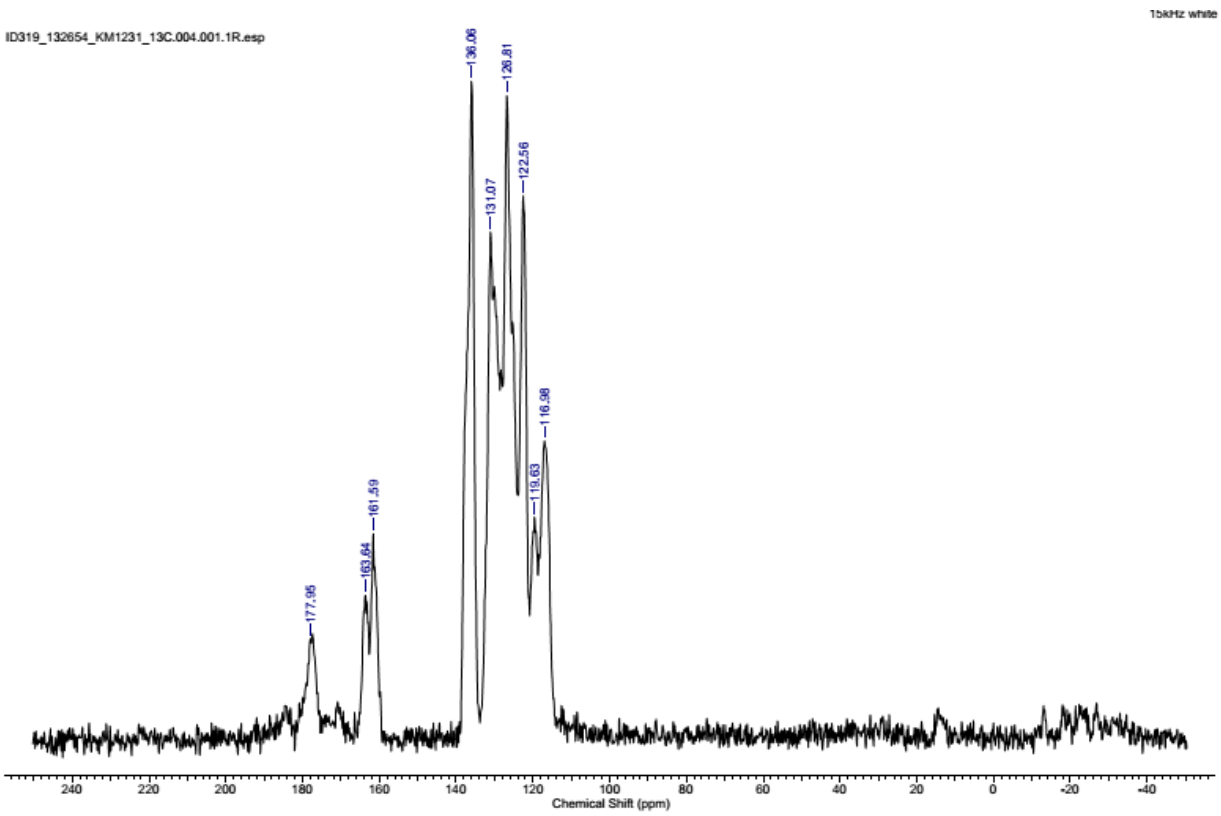

Figure S37. ^{13}C CP/MAS NMR spectrum of **5c** in solid state.

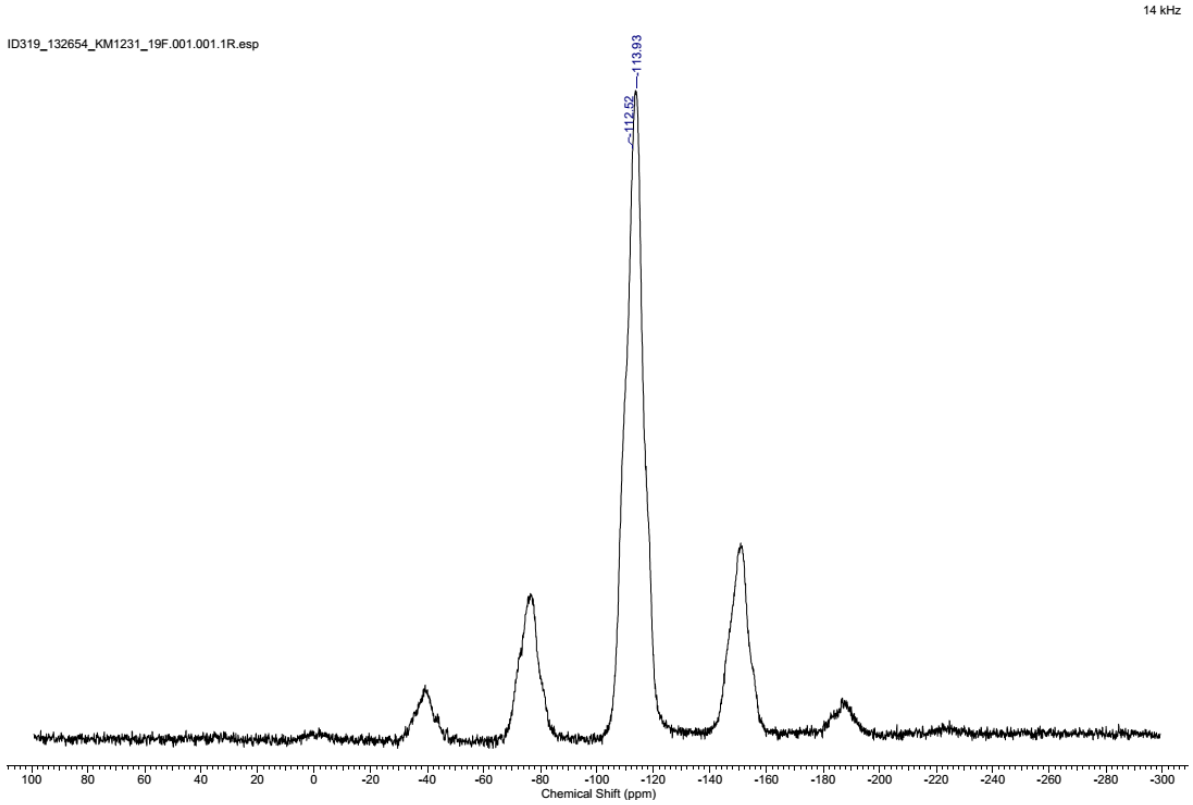

Figure S38. ^{19}F CP/MAS NMR spectrum of **5c** in solid state.

References

1. M. A. Kinzhalov, S. A. Timofeeva, K. V. Luzyanin, V. P. Boyarskiy, A. A. Yakimanskiy, M. Haukka, V. Y. Kukushkin. Palladium(II)-Mediated Addition of Benzenediamines to Isocyanides: Generation of Three Types of Diaminocarbene Ligands Depending on the Isomeric Structure of the Nucleophile. *Organometallics*, **2016**, *35*, 218–228.
2. M. A. Kinzhalov, A. A. Zolotarev, V. P. Boyarskiy. Crystal structure of cis-[PdCl2(CNMes)2]. *Journal of Structural Chemistry*, **2016**, *57*, 822–825.
3. I. M. Sluch, A. J. Miranda, O. Elbjeirami, M. A. Omary, L. M. Slaughter. Interplay of Metallophilic Interactions, π-π Stacking, and Ligand Substituent Effects in the Structures and Luminescence Properties of Neutral PtII and PdII Aryl Isocyanide Complexes. *Inorg. Chem.*, **2012**, *51*, 10728-10746.
4. M. V. Kashina, M. A. Kinzhalov, A. S. Smirnov, D. M. Ivanov, A. S. Novikov, V. Y. Kukushkin. Dihalomethanes as Bent Bifunctional XB/XB-Donating Building Blocks for Construction of Metal-involving Halogen Bonded Hexagons. *Chem. Asian J.*, **2019**, *14*, 3915–3920.
5. L. Palatinus, G. Chapuis. SUPERFLIP – a computer program for the solution of crystal structures by charge flipping in arbitrary dimensions. *J. Appl. Cryst.*, **2007**, *40*, 786–790.
6. G. M. Sheldrick. A short history of SHELX. *Acta Crystallogr.*, **2008**, *A64*, 112–122.
7. O. V. Dolomanov, L. J. Bourhis, R. J. Gildea, J. A. K. Howard, H. Puschmann. OLEX2: A complete structure solution, refinement and analysis program. *J. Appl. Cryst.*, **2009**, *42*, 339–341.
8. A. L. Spek. *Acta Cryst.*, **2009**, *D65*, 148-155.
9. C. Schmidt, L. Albrecht, S. Balasupramaniam, R. Misgeld, B. Karge, M. Brönstrup, A. Prokop, K. Baumann, S. Reichl, I. Ott. A gold(i) biscarbene complex with improved activity as a TrxR inhibitor and cytotoxic drug: comparative studies with different gold metallodrugs. *Metallomics*, **2019**, *11*, 533-545.
10. J. Eigner, P. Doty. The native, denatured and renatured states of deoxyribonucleic acid. *Journal of Molecular Biology*, **1965**, *12*, 549-580.
11. E. V. Frisman, L. V. Shchagina, V. I. Vorobev. A GLASS ROTATING VISCOMETER. *Biorheology*, **1965**, *2*, 189-94.
12. H. Yamakawa, M. Fujii. Intrinsic Viscosity of Wormlike Chains. Determination of the Shift Factor. *Macromolecules*, **1974**, *7*, 128-135.
13. E. V. Frisman, M. A. Sibileva, A. V. Krasnoperova. *Vysokomol. Soedin.* , **1962**, 597-606.
14. G. M. Morris, R. Huey, W. Lindstrom, M. F. Sanner, R. K. Belew, D. S. Goodsell, A. J. Olson. AutoDock4 and AutoDockTools4: Automated docking with selective receptor flexibility. *J Comput Chem*, **2009**, *30*, 2785-91.

15. P. Li, B. P. Roberts, D. K. Chakravorty, K. M. Merz. Rational Design of Particle Mesh Ewald Compatible Lennard-Jones Parameters for +2 Metal Cations in Explicit Solvent. *Journal of Chemical Theory and Computation*, **2013**, *9*, 2733-2748.

16. H. M. Berman, J. Westbrook, Z. Feng, G. Gilliland, T. N. Bhat, H. Weissig, I. N. Shindyalov, P. E. Bourne. The Protein Data Bank. *Nucleic Acids Research*, **2000**, *28*, 235-242.

17. M. J. Frisch, G. W. Trucks, H. B. Schlegel, G. E. Scuseria, M. A. Robb, J. R. Cheeseman, G. Scalmani, V. Barone, G. A. Petersson, H. Nakatsuji, X. Li, M. Caricato, A. V. Marenich, J. Bloino, B. G. Janesko, R. Gomperts, B. Mennucci, H. P. Hratchian, J. V. Ortiz, A. F. Izmaylov, J. L. Sonnenberg, Williams, F. Ding, F. Lipparini, F. Egidi, J. Goings, B. Peng, A. Petrone, T. Henderson, D. Ranasinghe, V. G. Zakrzewski, J. Gao, N. Rega, G. Zheng, W. Liang, M. Hada, M. Ehara, K. Toyota, R. Fukuda, J. Hasegawa, M. Ishida, T. Nakajima, Y. Honda, O. Kitao, H. Nakai, T. Vreven, K. Throssell, J. A. Montgomery Jr., J. E. Peralta, F. Ogliaro, M. J. Bearpark, J. J. Heyd, E. N. Brothers, K. N. Kudin, V. N. Staroverov, T. A. Keith, R. Kobayashi, J. Normand, K. Raghavachari, A. P. Rendell, J. C. Burant, S. S. Iyengar, J. Tomasi, M. Cossi, J. M. Millam, M. Klene, C. Adamo, R. Cammi, J. W. Ochterski, R. L. Martin, K. Morokuma, O. Farkas, J. B. Foresman, D. J. Fox, *Gaussian 16 Rev. C.01*. 2016: Wallingford, CT.

18. C. Adamo, V. Barone. Toward reliable density functional methods without adjustable parameters: The PBE0 model. *J. Chem. Phys.*, **1999**, *110*, 6158–6170.

19. P. J. Hay, W. R. Wadt. Ab initio effective core potentials for molecular calculations. Potentials for the transition metal atoms Sc to Hg. *The Journal of Chemical Physics*, **1985**, *82*, 270-283.

20. E. F. Pettersen, T. D. Goddard, C. C. Huang, G. S. Couch, D. M. Greenblatt, E. C. Meng, T. E. Ferrin. UCSF Chimera--a visualization system for exploratory research and analysis. *J Comput Chem*, **2004**, *25*, 1605-12.

21. Y. A. Wanniarachchi, L. M. Slaughter. One-step assembly of a chiral palladium bis(acyclic diaminocarbene) complex and its unexpected oxidation to a bis(amidine) complex *Chem. Commun.*, **2007**, *31*, 3294–3296.

22. K. V. Luzyanin, A. J. L. Pombeiro, M. Haukka, V. Y. Kukushkin. Coupling between 3-Iminoisoindolin-1-ones and Complexed Isonitriles as a Metal-mediated Route to a Novel Type of Palladium and Platinum Iminocarbene Species. *Organometallics*, **2008**, *27*, 5379–5389.

23. K. V. Luzyanin, A. G. Tskhovrebov, M. C. Carias, M. F. C. Guedes da Silva, A. J. L. Pombeiro, V. Y. Kukushkin. Novel Metal-Mediated (M = Pd, Pt) Coupling between Isonitriles and Benzophenone Hydrazone as a Route to Aminocarbene Complexes Exhibiting High Catalytic Activity (M = Pd) in the Suzuki−Miyaura Reaction. *Organometallics*, **2009**, *28*, 6559–6566.

24. A. G. Tskhovrebov, K. V. Luzyanin, F. M. Dolgushin, M. F. C. Guedes da Silva, A. J. L. Pombeiro, V. Y. Kukushkin. Novel reactivity mode of metal diaminocarbenes: palladium(II)-mediated coupling between acyclic diaminocarbenes and isonitriles leading to dinuclear species. *Organometallics*, **2011**, *30*, 3362–3370.

25. A. J. Martínez-Martínez, M. T. Chicote, D. Bautista, J. Vicente. Synthesis of Palladium(II), -(III), and -(IV) Complexes with Acyclic Diaminocarbene Ligands. *Organometallics*, **2012**, *31*, 3711–3719.

26. N. A. Kasyanenko, S. A. Prokhorova, E. F. Haya Enriquez, S. S. Sudakova, E. V. Frisman, S. A. Dyachenko, N. A. Smorygo, B. A. Ivin. Interaction of protonated DNA with trans-dichlorodiammineplatinum(II). *Colloids and Surfaces A: Physicochemical and Engineering Aspects*, **1999**, *148*, 121-128.

27. D. Suh, J. B. Chaires. Criteria for the mode of binding of DNA binding agents. *Bioorganic & Medicinal Chemistry*, **1995**, *3*, 723-728.

28. N. A. Kas'yanenko, S. S. Abramchuk, I. V. Blagodatskikh, A. A. Bogdanov, M. O. Gallyamov, A. I. Kononov, Y. V. Kosmotynskaya, N. L. Sitnikova, A. R. Khokhlov. Study of DNA complexation with platinum coordination compounds. *Polymer Science, Series A*, **2003**, *45*, 960-968.

29. D. M. Crothers. Calculation of binding isotherms for heterogeneous polymers. *Biopolymers*, **1968**, *6*, 575-584.

30. G. Maret, G. Weill. Magnetic birefringence study of the electrostatic and intrinsic persistence length of DNA. *Biopolymers*, **1983**, *22*, 2727-2744.

31. M. Sirajuddin, S. Ali, A. Badshah. Drug–DNA interactions and their study by UV–Visible, fluorescence spectroscopies and cyclic voltametry. *Journal of Photochemistry and Photobiology B: Biology*, **2013**, *124*, 1-19.

32. N. Kasyanenko, V. Bakulev, I. Perevyazko, T. Nekrasova, O. Nazarova, A. Slita, Y. Zolotova, E. Panarin. Model system for multifunctional delivery nanoplatforms based on DNA-Polymer complexes containing silver nanoparticles and fluorescent dye. *Journal of Biotechnology*, **2016**, *236*, 78-87.

33. S. Eriksson, S. K. Kim, M. Kubista, B. Norden. Binding of 4',6-diamidino-2-phenylindole (DAPI) to AT regions of DNA: Evidence for an allosteric conformational change. *Biochemistry*, **1993**, *32*, 2987-2998.

34. L. Strekowski, B. Wilson. Noncovalent interactions with DNA: An overview. *Mutation Research/Fundamental and Molecular Mechanisms of Mutagenesis*, **2007**, *623*, 3-13.

35. S. Dasari, P. Bernard Tchounwou. Cisplatin in cancer therapy: Molecular mechanisms of action. *European Journal of Pharmacology*, **2014**, *740*, 364-378.

36. C. G. Ricci, P. A. Netz. Docking Studies on DNA-Ligand Interactions: Building and Application of a Protocol To Identify the Binding Mode. *Journal of Chemical Information and Modeling*, **2009**, *49*, 1925-1935.

37. M. Á. Martínez, M. P. Carranza, A. Massaguer, L. Santos, J. A. Organero, C. Aliende, R. de Llorens, I. Ng-Choi, L. Feliu, M. Planas, A. M. Rodríguez, B. R. Manzano, G. Espino, F. A. Jalón. Synthesis and Biological Evaluation of Ru(II) and Pt(II) Complexes Bearing Carboxyl Groups as Potential Anticancer Targeted Drugs. *Inorganic Chemistry*, **2017**, *56*, 13679-13696.

38. C. Orvig, M. J. Abrams. Medicinal inorganic chemistry: introduction. *Chem Rev*, **1999**, *99*, 2201-4.

39. E. Meggers. Targeting proteins with metal complexes. *Chem Commun (Camb)*, **2009**, 1001-10.

40. K. L. Haas, K. J. Franz. Application of metal coordination chemistry to explore and manipulate cell biology. *Chem Rev*, **2009**, *109*, 4921-60.